Journal of the Mechanics and Physics of Solids 58 (2010) 1661–1680

Contents lists available at ScienceDirect

Journal of the Mechanics and Physics of Solids

journal homepage: www.elsevier.com/locate/jmps

A generic approach towards finite growth with examples of athlete's heart, cardiac dilation, and cardiac wall thickening

Serdar Göktepe [a], Oscar John Abilez [b,c], Ellen Kuhl [d,e,f,*]

[a] Department of Mechanical Engineering, 496 Lomita Mall, Stanford, CA 94305, USA
[b] Department of Bioengineering, 318W Campus Drive, Stanford, CA 94305, USA
[c] Department of Surgery, 318W Campus Drive, Stanford, CA 94305, USA
[d] Department of Mechanical Engineering, 496 Lomita Mall, Stanford, CA 94305, USA
[e] Department of Bioengineering, 496 Lomita Mall, Stanford, CA 94305, USA
[f] Department of Cardiothoracic Surgery, 496 Lomita Mall, Stanford, CA 94305, USA

ARTICLE INFO

Article history:
Received 17 February 2010
Received in revised form
25 June 2010
Accepted 1 July 2010

Keywords:
Biological growth
Biological material
Constitutive behavior
Finite elements
Numerical algorithms

ABSTRACT

The objective of this work is to establish a generic continuum-based computational concept for finite growth of living biological tissues. The underlying idea is the introduction of an incompatible growth configuration which naturally introduces a multiplicative decomposition of the deformation gradient into an elastic and a growth part. The two major challenges of finite growth are the kinematic characterization of the growth tensor and the identification of mechanical driving forces for its evolution. Motivated by morphological changes in cell geometry, we illustrate a micromechanically motivated ansatz for the growth tensor for cardiac tissue that can capture both strain-driven ventricular dilation and stress-driven wall thickening. Guided by clinical observations, we explore three distinct pathophysiological cases: athlete's heart, cardiac dilation, and cardiac wall thickening. We demonstrate the computational solution of finite growth within a fully implicit incremental iterative Newton–Raphson based finite element solution scheme. The features of the proposed approach are illustrated and compared for the three different growth pathologies in terms of a generic bi-ventricular heart model.

1. Motivation

Unlike engineering materials, living biological tissues are known to grow and adaptively change their form and function in response to environmental changes. Almost a century ago, it was recognized that the physical laws of mechanics could provide a natural framework to characterize relations between form and function of growing biological structures (Thompson, 1917). Since the classical framework of continuum thermodynamics has originally been developed for non-living materials, however, we have now come to realize that the traditional kinematic equations, the balance equations, and the constitutive equations have to be reconsidered in the presence of growth (Cowin and Hegedus, 1976; Hsu, 1968; Humphrey and Rajagopal, 2002; Kuhl and Steinmann, 2003a, 2003b; Skalak, 1981). Deviations from the classical theory strongly depend on the particular type of biological adaptation (Cowin, 2004; Taber, 1995). We commonly distinguish

* Corresponding author at: Department of Mechanical Engineering, 496 Lomita Mall, Stanford, CA 94305, USA. Tel.: +1 650 450 0855; fax: +1 650 725 1587.
E-mail addresses: goktepe@stanford.edu (S. Göktepe), ojabilez@stanford.edu (O.J. Abilez), ekuhl@stanford.edu (E. Kuhl).
URL: http://biomechanics.stanford.edu (E. Kuhl).

0022-5096/$ - see front matter © 2010 Elsevier Ltd. All rights reserved.
doi:10.1016/j.jmps.2010.07.003

between density growth common to hard tissues such as bone (Carter and Hayes, 1977; Cowin and Hegedus, 1976; Kuhl et al., 2003; Kuhl and Steinmann, 2003c), tip growth common to plants (Dumais et al., 2006), surface growth common to sea shells or horns (Skalak et al., 1997; Thompson, 1917), volume growth common to soft tissues such as arteries or tumors (Ambrosi and Mollica, 2002; Rodriguez et al., 1994; Taber and Humphrey, 2001), and remodeling common to the development of soft collageneous tissues (Ciarletta and Ben Amar, 2009; Himpel et al., 2008; Kuhl et al., 2005; Kuhl and Holzapfel, 2007; Menzel, 2005).

In this manuscript, we shall focus exclusively on volume growth which has experienced its breakthrough in continuum modeling with the introduction of an incompatible growth configuration and the corresponding multiplicative decomposition of the deformation gradient into an elastic and a growth part (Rodriguez et al., 1994), a concept that was originally developed for finite strain plasticity (Lee, 1969). Today, there seems to be a general agreement that the concept of an incompatible growth configuration is a suitable and effective approach towards finite growth, and a tremendous amount of research has been devoted to establish continuum theories of finite growth within the last decade (Ambrosi et al., 2008, under review; Ben Amar and Goriely, 2005; Chen and Hoger, 2000; Epstein and Maugin, 2000; Goriely and Ben Amar, 2007; Imatani and Maugin, 2002; Lubarda and Hoger, 2002). The theory of finite growth has been successfully applied to characterize growth of tendon (Garikipati et al., 2004), tumors (Ambrosi and Mollica, 2002), cartilage (Klisch et al., 2003), vascular tissue (Humphrey, 2002, 2008; Kuhl et al., 2007; Taber and Humphrey, 2001), and, most recently, cardiac tissue (Kroon et al., 2009; Göktepe et al., 2010a). While initial efforts have mainly been theoretical in nature (Ambrosi and Mollica, 2002; Garikipati, 2009; Humphrey, 2002; Taber and Humphrey, 2001), we can clearly observe a trend towards analyzing inhomogeneous finite growth based on computational modeling (Alastrue et al., 2009; Alford and Taber, 2008; Figueroa et al., 2009; Himpel et al., 2005; Kroon et al., 2009), usually by introducing the growth tensor as an internal variable within a finite element framework. Despite tremendous research aiming to provide a better understanding of the mechanics of growth, two fundamental questions still remain unanswered: How do we define an appropriate kinematic characterization of the growth tensor? And how do we identify mechanical driving forces for growth?

The main idea of this manuscript is to closely tie the definition of the macroscopic growth tensor and the forces driving its evolution to microstructural observations. Since the cellular microstructure can vary considerably for different types of tissue, we focus on one particular model system, the human heart, and tie its growth characterization to morphological changes in its key characteristic cell type, the cardiomyocyte. Although cardiomyocytes comprise only one-fourth of the total number of cells in the heart, they account for more than 90% of the volume of the cardiac muscle (Kumar et al., 2005). The functional contractile unit of the cardiomyocyte is the sarcomere, a $1.6-2.2\,\mu m$ long parallel arrangement of thick filaments of myosin that slide along thin filaments of actin. About 50 sarcomeres in series make up a myofibril and about 50–100 myofibrils in parallel make up a cardiomyocyte. Healthy cardiomyocytes have a cylindrical shape with a diameter of $10-25\,\mu m$ and a length of $100\,\mu m$ (Opie, 2003), consisting of approximately 5000 sarcomere units. Unlike most other cell types in the human body, functional adult cardiomyocytes cannot perform cell division (hyperplasia) such that the total number of cells, about 6 billion at birth, cannot increase. However, cardiomyocytes can grow in size (hypertrophy), and they do so by the deposition of new sarcomere units. The muscle fibers of cardiomyocytes are arranged in transmural layers or sheets which are organized helically around the heart. Fig. 1 illustrates the orthotropic architecture of the mycoardium in terms of the fiber directions $\boldsymbol{f}_0$ and sheet plane vectors $\boldsymbol{s}_0$.

We hypothesize that macrostructural maladaptive cardiac growth can be traced to the intrinsic microstructural architecture of the cardiomyocyte itself. Two classical examples are eccentric and concentric hypertrophy (Libby et al., 2007; Opie, 2003). In response to chronic volume overload, an increased diastolic wall stress leads to the addition of sarcomeres in series, resulting in a relative increase in cardiomyocyte length, associated with eccentric hypertrophy and ventricular dilation. In response to chronic pressure overload, however, an increased systolic wall stress leads to the

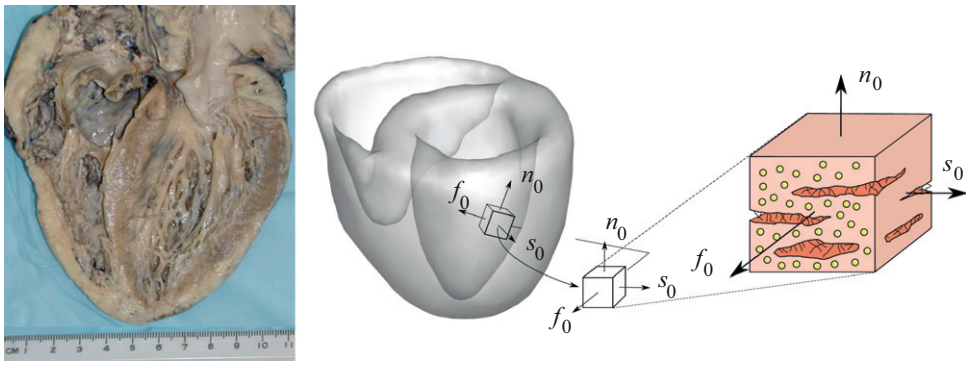

Fig. 1. Normal healthy heart, courtesy of Chengpei Xu (left). Microstructural architecture of the heart (right). The orthogonal unit vectors $\boldsymbol{f}_0$ and $\boldsymbol{s}_0$ designate the muscle fiber direction and the sheet plane vector in the undeformed configuration. The orthogonal vector $\boldsymbol{n}_0$ completes the local coordinate system, where the constitutive response of the heart is typically viewed as orthotropic.

addition of sacromeres in parallel, resulting in a relative increase in myocyte cross sectional area, associated with concentric hypertrophy and ventricular wall thickening (Emmanouilides et al., 1994; Kumar et al., 2005; Taber, 1995). Both forms of maladaptive growth are illustrated in Fig. 2 and their mechanical characteristics are summarized in Fig. 3. They lead to significant changes in phenotype, secondary to the reactivation of portfolios of genes that are normally expressed post-natally and that are correlated with contractile dysfunction (Hunter and Chien, 1999).

Cardiac growth can be either healthy and normal (physiologic) or unhealthy and diseased (pathologic), either reversible or irreversible. Within this manuscript, we model three of the most common cases of mechanically driven cardiac growth: (i) athlete's heart characterized by physiological, reversible, stress-driven isotropic growth (Ekblom and Hermansen, 1968; Mihl et al., 2008; Pluim et al., 2000), (ii) cardiac dilation characterized by pathological, irreversible, strain-driven transversely isotropic longitudinal growth (Berne and Levy, 2001; Cheng et al., 2006; Kumar et al., 2005; Opie, 2003), and (iii) cardiac wall thickening characterized by pathological, irreversible, stress-driven transversely isotropic transverse growth (Kumar et al., 2005; Maron and McKenna, 2003; Opie, 2003). Since the focus of this manuscript is on generic micromechanically motivated finite growth, we model the baseline properties of cardiac tissue as isotropic and passive. However, we are currently exploring more physiological orthotropic models for passive myocardial tissue (Göktepe et al., 2010b; Holzapfel and Ogden, 2009), and the incorporation of an active material response (Göktepe and Kuhl, 2009, 2010; Kotikanyadanam et al., 2010) in combination with cardiac growth.

This manuscript is organized as follows. In Section 2 we outline the generic continuous equations for finite growth based on the kinematic equations, the balance equations, and the constitutive equations. Section 3 then addresses the generic computational realization within a nonlinear finite element setting, with particular focus on the consistent linearization and the underlying local and global Newton iteration. In Section 4 we briefly summarize a prototype biventricular heart model that we will utilize to compare the different growth pathologies discussed in the next three sections. We then specify the generic growth model of Sections 2 and 3 to characterize the adaptation of the heart in three

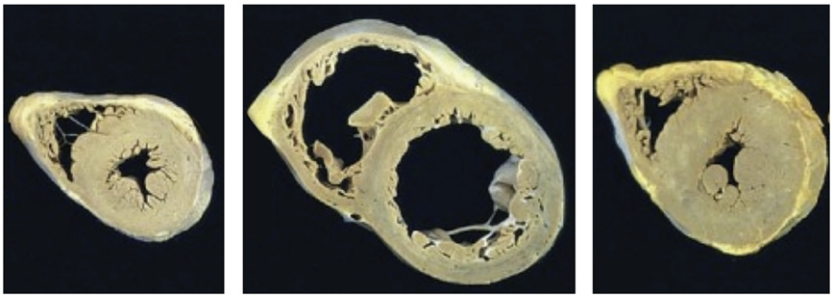

Fig. 2. Pathophysiology of maladaptive growth of the heart viewed in transverse heart sections, reprinted with permission from Emmanouilides et al. (1994) and Kumar et al. (2005). Compared with the normal heart (left), eccentric hypertrophy is associated with ventricular dilation in response to volume overload (center). Concentric hypertrophy is associated with ventricular wall thickening in response to pressure overload (right).

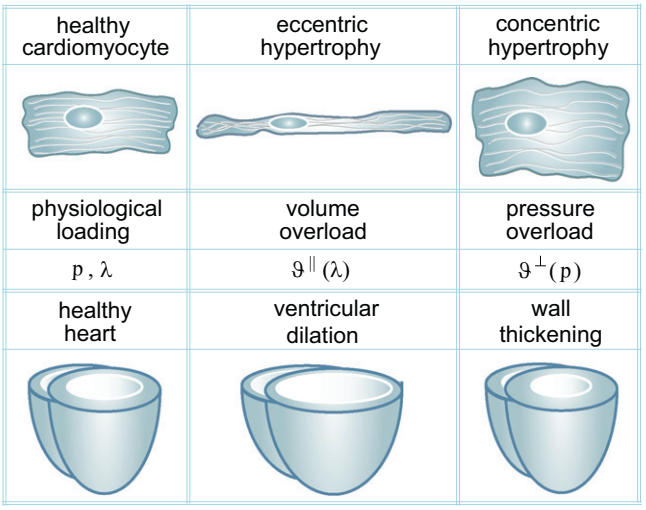

Fig. 3. Microscopic growth of cardiomyocytes vs. macroscopic growth of the heart. Compared with the normal heart (left), eccentric hypertrophy is associated with ventricular dilation in response to volume overload (center). Concentric hypertrophy is associated with ventricular wall thickening in response to pressure overload (right).

specific microstructurally motivated case studies. Section 5 illustrates stress-driven isotropic growth characteristic for athlete's heart. Section 6 documents strain-driven transversely isotropic longitudinal growth characteristic for cardiac dilation. Section 7 illustrates stress-driven transversely isotropic transverse growth characteristic for cardiac wall thickening. Finally, Section 8 concludes with a critical discussion of the proposed microstructurally motivated approach towards finite growth and its potential in life sciences and medicine.

2. Continuous equations of finite growth

In this section, we illustrate the governing equations for finite growth which consist of three basic sets of equations: (i) the kinematic equations, which utilize the concept of an incompatible growth configuration and the multiplicative decomposition of the deformation gradient; (ii) the balance equations, which are only indirectly affected by the growth process and thus take their standard format in the reference or deformed configuration; and (iii) the constitutive equations, which define the baseline elastic response in the intermediate configuration, supplemented by an appropriate definition of the growth tensor and its evolution equation to characterize different forms of growth.

2.1. Kinematics of finite growth

Within the framework of finite growth, the key kinematic assumption is the multiplicative decomposition of deformation gradient $\boldsymbol{F}$ into an elastic part $\boldsymbol{F}^{\mathrm{e}}$ and a growth part $\boldsymbol{F}^{\mathrm{g}}$ (Rodriguez et al., 1994),

$$\boldsymbol{F}=\boldsymbol{F}^{\mathrm{e}}\cdot\boldsymbol{F}^{\mathrm{g}} \quad \text{with } \boldsymbol{F}=\nabla_{\boldsymbol{X}}\boldsymbol{\varphi}, \tag{1}$$

adapting a concept first proposed in the context of finite elasto-plasticity (Lee, 1969). The Jacobians of the deformation gradient and its elastic and growth counterparts will be denoted as $J=\det(\boldsymbol{F})$, $J^{\mathrm{e}}=\det(\boldsymbol{F}^{\mathrm{e}})$, and $J^{\mathrm{g}}=\det(\boldsymbol{F}^{\mathrm{g}})$, respectively, such that $J=J^{\mathrm{e}}J^{\mathrm{g}}$. We can then introduce the right Cauchy Green tensor $\boldsymbol{C}$, and, in complete analogy, the elastic right Cauchy Green tensor $\boldsymbol{C}^{\mathrm{e}}$ as covariant pull backs of the covariant spatial metric $\boldsymbol{g}$ to the undeformed reference configuration and to the intermediate configuration, respectively.

$$\boldsymbol{C}=\boldsymbol{F}^{\mathrm{t}}\cdot\boldsymbol{g}\cdot\boldsymbol{F}, \quad \boldsymbol{C}^{\mathrm{e}}=\boldsymbol{F}^{\mathrm{et}}\cdot\boldsymbol{g}\cdot\boldsymbol{F}^{\mathrm{e}}=\boldsymbol{F}^{\mathrm{g-t}}\cdot\boldsymbol{C}\cdot\boldsymbol{F}^{\mathrm{g-1}}. \tag{2}$$

Recall that in our case of Cartesian coordinates, $\boldsymbol{g}$ is equal to the identity tensor. The spatial velocity gradient $\boldsymbol{l}$ then takes the following multiplicative representation:

$$\boldsymbol{l}=\dot{\boldsymbol{F}}\cdot\boldsymbol{F}^{-1} \quad \text{with } \boldsymbol{l}=\nabla_{x}\boldsymbol{v}, \tag{3}$$

in terms of the velocity $\boldsymbol{v}=\dot{\boldsymbol{\varphi}}$, where $\{\dot{\circ}\}=\partial_{\mathrm{t}}\{\circ\}|_{\boldsymbol{X}}$ denotes the time derivative at fixed material position $\boldsymbol{X}$. The symmetric part of the spatial velocity gradient defines the spatial rate of deformation tensor $\boldsymbol{d}=(\boldsymbol{g}\cdot\boldsymbol{l})^{\mathrm{sym}}$. Recall that the pull back of the spatial velocity gradient to the intermediate configuration

$$\boldsymbol{F}^{\mathrm{e-1}}\cdot\boldsymbol{l}\cdot\boldsymbol{F}^{\mathrm{e}}=\boldsymbol{L}^{\mathrm{e}}+\boldsymbol{L}^{\mathrm{g}} \tag{4}$$

results in its additive decomposition into the elastic velocity gradient $\boldsymbol{L}^{\mathrm{e}}$ and the growth velocity gradient $\boldsymbol{L}^{\mathrm{g}}$

$$\boldsymbol{L}^{\mathrm{e}}=\boldsymbol{F}^{\mathrm{e-1}}\cdot\dot{\boldsymbol{F}}^{\mathrm{e}}, \quad \boldsymbol{L}^{\mathrm{g}}=\dot{\boldsymbol{F}}^{\mathrm{g}}\cdot\boldsymbol{F}^{\mathrm{g-1}}, \tag{5}$$

such that the rate of deformation tensor of the intermediate configuration can be expressed as $\boldsymbol{d}^{\mathrm{g}}=(\boldsymbol{g}\cdot\boldsymbol{l}^{\mathrm{g}})^{\mathrm{sym}}$ with $\boldsymbol{l}^{\mathrm{g}}=\boldsymbol{F}^{\mathrm{e}}\cdot\boldsymbol{L}^{\mathrm{g}}\cdot\boldsymbol{F}^{\mathrm{e-1}}$. Fig. 4 illustrates the kinematics of finite growth in terms of the covariant spatial metric $\boldsymbol{g}$, the deformation tensors $\boldsymbol{C}$ and $\boldsymbol{C}^{\mathrm{e}}$, and the mappings $\boldsymbol{F}=\boldsymbol{F}^{\mathrm{e}}\cdot\boldsymbol{F}^{\mathrm{g}}$ and $\boldsymbol{F}^{-\mathrm{t}}=\boldsymbol{F}^{\mathrm{e-t}}\cdot\boldsymbol{F}^{\mathrm{g-t}}$ between tangent spaces $T\mathcal{B}$ and cotangent spaces $T^{*}\mathcal{B}$ in the material configuration, the intermediate configuration, and the spatial configuration.

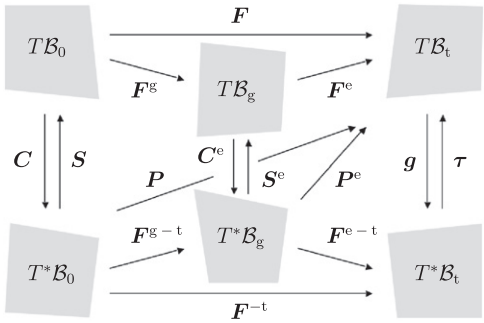

Fig. 4. Kinematics of finite growth. Illustration of covariant spatial metric $\boldsymbol{g}$, deformation tensors $\boldsymbol{C}$ and $\boldsymbol{C}^{\mathrm{e}}$, stress tensors $\boldsymbol{S}$, $\boldsymbol{P}$, $\boldsymbol{P}^{\mathrm{e}}$ and $\boldsymbol{\tau}$, and mappings $\boldsymbol{F}=\boldsymbol{F}^{\mathrm{e}}\cdot\boldsymbol{F}^{\mathrm{g}}$ and $\boldsymbol{F}^{-\mathrm{t}}=\boldsymbol{F}^{\mathrm{e-t}}\cdot\boldsymbol{F}^{\mathrm{g-t}}$ between tangent spaces $T\mathcal{B}$ and cotangent spaces $T^{*}\mathcal{B}$ in the material configuration, the intermediate configuration, and the spatial configuration.

2.2. Balance equations of finite growth

In the absence of transient terms and external forces, the balance of linear momentum can be expressed in the following three common formats:

$$\mathrm{Div}(\boldsymbol{F}\cdot\boldsymbol{S})=\boldsymbol{0},\quad \mathrm{Div}\,(\boldsymbol{P})=\boldsymbol{0},\quad \mathrm{div}\,(J^{-1}\boldsymbol{\tau})=\boldsymbol{0}, \tag{6}$$

where $\boldsymbol{S}=\boldsymbol{F}^{-1}\cdot\boldsymbol{P}$ is the second Piola Kirchhoff stress, $\boldsymbol{P}$ is the Piola stress, and $\boldsymbol{\tau}=\boldsymbol{P}\cdot\boldsymbol{F}^{\mathrm{t}}$ is the Kirchhoff stress, respectively. In the above expressions, $\mathrm{Div}\{\circ\}=\partial\{\circ\}/\partial\boldsymbol{X}$ and $\mathrm{div}\{\circ\}=\partial\{\circ\}/\partial\boldsymbol{\varphi}$ denote the material and spatial divergence, i.e., the derivative with respect to the material and spatial position $\boldsymbol{X}$ and $\boldsymbol{\varphi}$. Moreover, using standard arguments of thermodynamics, we can introduce the balance of energy and transform it into the dissipation inequality

$$\mathcal{D}=\boldsymbol{S}:\tfrac{1}{2}\dot{\boldsymbol{C}}-\dot{\psi}-\mathcal{S}_0=\tilde{\boldsymbol{P}}:\dot{\boldsymbol{F}}-\dot{\psi}-\mathcal{S}_0=\boldsymbol{\tau}:\boldsymbol{d}-\dot{\psi}-\mathcal{S}_0\geq 0, \tag{7}$$

which, for the sake of completeness, has again been stated in its three most common formats. It should be observed that $\tilde{\boldsymbol{P}}$ denotes the mixed-variant Piola stress tensor, defined by $\tilde{\boldsymbol{P}}:=\boldsymbol{g}\cdot\boldsymbol{P}$. To account for a potential material strengthening characteristic for growing biological tissue, we have introduced the extra entropy source $\mathcal{S}_0$ in the undeformed configuration.

2.3. Constitutive equations of finite growth

In general, the constitutive equations for finite growth consist of three assumptions: (i) the definition of the stresses $\boldsymbol{S}$, $\boldsymbol{P}$, or $\boldsymbol{\tau}$, which can be conveniently be derived as energetically conjugate to the corresponding total kinematic quantities $\boldsymbol{C}$, $\boldsymbol{F}$, or $\boldsymbol{g}$ via the evaluation of the dissipation inequality; (ii) the definition the growth tensor $\boldsymbol{F}^{\mathrm{g}}$, which can be either compressible or incompressible, either isotropic or anisotropic taking into account the characteristic material microstructure, and (iii) the definition of a set of evolution equations for the internal variables that characterize the growth process which can be either irreversible or reversible, either stress- or strain-driven. For the sake of transparency, let us assume an isotropic elastic response that can be characterized exclusively in terms of the right Cauchy Green tensor of the intermediate configuration $\boldsymbol{C}^{\mathrm{e}}=\boldsymbol{F}^{\mathrm{g-t}}\cdot\boldsymbol{C}\cdot\boldsymbol{F}^{\mathrm{g}-1}$, the elastic part of the deformation gradient $\boldsymbol{F}^{\mathrm{e}}=\boldsymbol{F}\cdot\boldsymbol{F}^{\mathrm{g}-1}$, or the elastic right Cauchy Green tensor expressed in the following format $\boldsymbol{C}^{\mathrm{e}}=\boldsymbol{F}^{\mathrm{et}}\cdot\boldsymbol{g}\cdot\boldsymbol{F}^{\mathrm{e}}$. Following standard concepts of thermodynamics, we can then introduce the Helmholtz free energy ψ,

$$\psi=\hat{\psi}(\boldsymbol{C},\boldsymbol{F}^{\mathrm{g}}),\quad \psi=\hat{\psi}(\boldsymbol{F},\boldsymbol{F}^{\mathrm{g}}),\quad \psi=\hat{\psi}(\boldsymbol{g},\boldsymbol{F}^{\mathrm{e}}) \tag{8}$$

and evaluate the dissipation inequality (7)

$$\mathcal{D}=\boldsymbol{S}:\frac{1}{2}\dot{\boldsymbol{C}}-\dot{\psi}-\mathcal{S}_0=\left[\boldsymbol{S}-2\frac{\partial\psi}{\partial\boldsymbol{C}}\right]:\frac{1}{2}\dot{\boldsymbol{C}}+\boldsymbol{M}^{\mathrm{e}}:\boldsymbol{L}^{\mathrm{g}}-\mathcal{S}_0\geq 0,$$

$$\mathcal{D}=\tilde{\boldsymbol{P}}:\dot{\boldsymbol{F}}-\dot{\psi}-\mathcal{S}_0=\left[\tilde{\boldsymbol{P}}-\frac{\partial\psi}{\partial\boldsymbol{F}}\right]:\dot{\boldsymbol{F}}+[\boldsymbol{F}^{\mathrm{et}}\cdot\tilde{\boldsymbol{P}}]:\dot{\boldsymbol{F}}^{\mathrm{g}}-\mathcal{S}_0\geq 0,$$

$$\mathcal{D}=\boldsymbol{\tau}:\dot{\boldsymbol{d}}-\dot{\psi}-\mathcal{S}_0=\left[\boldsymbol{\tau}-2\frac{\partial\psi}{\partial\boldsymbol{g}}\right]:\boldsymbol{d}+\boldsymbol{\tau}:\boldsymbol{d}^{\mathrm{g}}-\mathcal{S}_0\geq 0 \tag{9}$$

to obtain the definitions for the second Piola–Kirchhoff stress $\boldsymbol{S}$, the Piola stress $\boldsymbol{P}$, and the Kirchhoff stress $\boldsymbol{\tau}$ as thermodynamically conjugate quantities to the elastic right Cauchy Green deformation tensor $\boldsymbol{C}^{\mathrm{e}}$, to the elastic part of the deformation gradient $\boldsymbol{F}^{\mathrm{e}}$, and to the spatial metric $\boldsymbol{g}$, respectively:

$$\boldsymbol{S}=2\frac{\partial\psi}{\partial\boldsymbol{C}}=2\frac{\partial\psi}{\partial\boldsymbol{C}^{\mathrm{e}}}:\frac{\partial\boldsymbol{C}^{\mathrm{e}}}{\partial\boldsymbol{C}}=\boldsymbol{F}^{\mathrm{g}-1}\cdot\boldsymbol{S}^{\mathrm{e}}\cdot\boldsymbol{F}^{\mathrm{g-t}}\boldsymbol{S}^{\mathrm{e}}:=\frac{\partial\psi}{\partial\boldsymbol{C}^{\mathrm{e}}},$$

$$\tilde{\boldsymbol{P}}=\frac{\partial\psi}{\partial\boldsymbol{F}}=\frac{\partial\psi}{\partial\boldsymbol{F}^{\mathrm{e}}}:\frac{\partial\boldsymbol{F}^{\mathrm{e}}}{\partial\boldsymbol{F}}=\tilde{\boldsymbol{P}^{\mathrm{e}}}\cdot\boldsymbol{F}^{\mathrm{g-t}}\tilde{\boldsymbol{P}^{\mathrm{e}}}:=\frac{\partial\psi}{\partial\boldsymbol{F}^{\mathrm{e}}},$$

$$\boldsymbol{\tau}=2\frac{\partial\psi}{\partial\boldsymbol{g}}=\boldsymbol{F}^{\mathrm{e}}\cdot\boldsymbol{S}^{\mathrm{e}}\cdot\boldsymbol{F}^{\mathrm{et}}\boldsymbol{\tau}:=2\frac{\partial\psi}{\partial\boldsymbol{g}}. \tag{10}$$

As a side remark, the elastic constitutive moduli $\mathbf{L}^{\mathrm{e}}$, $\mathbf{A}^{\mathrm{e}}$, and $\mathbf{e}^{\mathrm{e}}$, can be obtained by taking the second derivative of the Helmholtz free energy ψ with respect to the corresponding kinematic quantities $\boldsymbol{C}^{\mathrm{e}}$, $\boldsymbol{F}^{\mathrm{e}}$, and $\boldsymbol{g}$:

$$\mathbf{L}^{\mathrm{e}}=2\frac{\partial\boldsymbol{S}^{\mathrm{e}}}{\partial\boldsymbol{C}^{\mathrm{e}}}=4\frac{\partial^2\psi}{\partial\boldsymbol{C}^{\mathrm{e}}\otimes\partial\boldsymbol{C}^{\mathrm{e}}},$$

$$\mathbf{A}^{\mathrm{e}}=\frac{\partial\tilde{\boldsymbol{P}^{\mathrm{e}}}}{\partial\boldsymbol{F}^{\mathrm{e}}}=\frac{\partial^2\psi}{\partial\boldsymbol{F}^{\mathrm{e}}\otimes\partial\boldsymbol{F}^{\mathrm{e}}},$$

$$\mathbf{e}^{\mathrm{e}} = 2\frac{\partial \boldsymbol{\tau}}{\partial \boldsymbol{g}} = 4\frac{\partial^2 \psi}{\partial \boldsymbol{g} \otimes \partial \boldsymbol{g}}. \tag{11}$$

With this set of equations completing the definition of the elastic constitutive response, we would like to re-iterate that the concept of finite growth resembles finite strain plasticity in the sense that the basic constitutive equations themselves remain unchanged, however, they are evaluated exclusively in terms of the kinematic quantities of the intermediate configuration. Next, we define the growth tensor $\boldsymbol{F}^{\mathrm{g}}$, adopting the common assumption of symmetry, i.e., $\boldsymbol{F}^{\mathrm{g}} = \boldsymbol{F}^{\mathrm{gt}}$. Taking into account the orthotropic nature of most biological tissue, we introduce the growth tensor in the following generic format:

$$\boldsymbol{F}^{\mathrm{g}} = \vartheta^{\mathrm{f}} \boldsymbol{f}_0 \otimes \boldsymbol{f}_0 + \vartheta^{\mathrm{s}} \boldsymbol{s}_0 \otimes \boldsymbol{s}_0 + \vartheta^{\mathrm{n}} \boldsymbol{n}_0 \otimes \boldsymbol{n}_0, \tag{12}$$

where $\boldsymbol{f}_0$, $\boldsymbol{s}_0$, and $\boldsymbol{n}_0$ are the unit vectors of the orthotropic microstructure in the reference configuration and $\boldsymbol{\vartheta}^{\mathrm{g}} = [\vartheta^{\mathrm{f}}, \vartheta^{\mathrm{s}}, \vartheta^{\mathrm{n}}]$ denotes the set of internal variables which are often referred to as growth multipliers. These take the value one in the plain elastic case, are smaller than one for shrinkage and larger than one for growth. To complete the set of constitutive equations, we need to specify the evolution of the internal variables $\dot{\boldsymbol{\vartheta}}^{\mathrm{g}}$. A common format is to introduce mechanically driven growth criteria $\boldsymbol{\phi}^{\mathrm{g}}$ which are only activated if a mechanical driving force exceeds a certain physiological threshold level such that $\boldsymbol{\phi}^{\mathrm{g}} > \mathbf{0}$. The growth criteria are typically weighted by a matrix of growth functions $\boldsymbol{k}^{\mathrm{g}}(\boldsymbol{\vartheta}^{\mathrm{g}})$ to ensure that the material does not grow unboundedly. It is worth noting that the matrix $\boldsymbol{k}^{\mathrm{g}}(\boldsymbol{\vartheta}^{\mathrm{g}})$ is usually diagonal, meaning that the evolution equations for the growth multipliers $\boldsymbol{\vartheta}^{\mathrm{g}}$ would be fully decoupled.

$$\dot{\boldsymbol{\vartheta}}^{\mathrm{g}} = \boldsymbol{k}^{\mathrm{g}}(\boldsymbol{\vartheta}^{\mathrm{g}}) \cdot \boldsymbol{\phi}^{\mathrm{g}}(\boldsymbol{F}^{\mathrm{e}}) \quad \text{or} \quad \dot{\boldsymbol{\vartheta}}^{\mathrm{g}} = \boldsymbol{k}^{\mathrm{g}}(\boldsymbol{\vartheta}^{\mathrm{g}}) \cdot \boldsymbol{\phi}^{\mathrm{g}}(\boldsymbol{M}^{\mathrm{e}}). \tag{13}$$

A limiting growth function that has been proposed in the literature (Lubarda and Hoger, 2002), $k^{\mathrm{g}}(\vartheta^{\mathrm{g}}) = [[\vartheta^{\max} - \vartheta^{\mathrm{g}}]/[\vartheta^{\max} - 1]]^{\gamma}/\tau$, is illustrated in Fig. 5. For this function, the growth rate decays smoothly until the growth multiplier ϑ^{g} has reached its maximum value $\vartheta^{\max}$, while the nonlinearity of the growth process and the growth speed are governed through γ and τ, respectively. Mechanically driven growth processes can either be strain- or stress-driven. For the strain-driven case, the growth criterion $\boldsymbol{\phi}^{\mathrm{g}}(\boldsymbol{F}^{\mathrm{e}})$ can be expressed in terms of the elastic part of the deformation gradient, in analogy to finite strain damage. For the stress-driven case, the growth criterion $\boldsymbol{\phi}^{\mathrm{g}}(\boldsymbol{M}^{\mathrm{e}})$, can be expressed in terms of the Mandel stress of the intermediate configuration, $\boldsymbol{M}^{\mathrm{e}} = \boldsymbol{C}^{\mathrm{e}} \cdot \boldsymbol{S}^{\mathrm{e}}$, motivated by the dissipation inequality (9), in analogy to finite strain plasticity. Particular choices of growth tensors (12) and evolution equations (13) will be specified in the example Sections 5–7.

Remark 1 (*Baseline elasticity*). To focus on the impact of growth, we assume a generic isotropic Neo-Hookean baseline elasticity throughout this manuscript, and specify the free energy of Eq. (8) as follows:

$$\psi = \tfrac{1}{2}\lambda \ln^2(J^{\mathrm{e}}) + \tfrac{1}{2}\mu[\boldsymbol{C}^{\mathrm{e}} : \boldsymbol{I} - 3 - 2\ln(J^{\mathrm{e}})].$$

According to Eq. (10), the elastic second Piola Kirchhoff stress $\boldsymbol{S}^{\mathrm{e}} = 2\partial\psi/\partial\boldsymbol{C}^{\mathrm{e}}$ can then be expressed as

$$\boldsymbol{S}^{\mathrm{e}} = [\lambda \ln(J^{\mathrm{e}}) - \mu]\boldsymbol{C}^{\mathrm{e}-1} + \mu\boldsymbol{I},$$

and the elastic constitutive moduli $\mathbf{L}^{\mathrm{e}} = 2\partial\boldsymbol{S}^{\mathrm{e}}/\partial\boldsymbol{C}^{\mathrm{e}}$ introduced in Eq. (11) take the following explicit representation:

$$\mathbf{L}^{\mathrm{e}} = \lambda \boldsymbol{C}^{\mathrm{e}-1} \otimes \boldsymbol{C}^{\mathrm{e}-1} + [\mu - \lambda \ln(J^{\mathrm{e}})][\boldsymbol{C}^{\mathrm{e}} \overline{\otimes} \boldsymbol{C}^{\mathrm{e}} + \boldsymbol{C}^{\mathrm{e}} \underline{\otimes} \boldsymbol{C}^{\mathrm{e}}].$$

However, the incorporation of more sophisticated anisotropic constitutive equations for the baseline elastic response of cardiac muscle (Göktepe et al., 2010b; Holzapfel and Ogden, 2009) is extremely straightforward as it only affects the calculation of the elastic stresses $\boldsymbol{S}^{\mathrm{e}}$ and the corresponding elastic contributions to the constitutive moduli $\mathbf{L}^{\mathrm{e}}$.

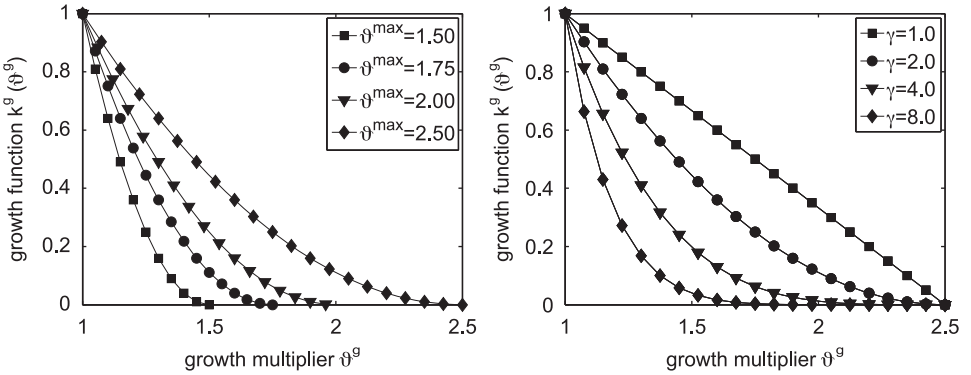

Fig. 5. Typical example of growth function $k^{\mathrm{g}}(\vartheta^{\mathrm{g}}) = [[\vartheta^{\max} - \vartheta^{\mathrm{g}}]/[\vartheta^{\max} - 1]]^{\gamma}/\tau$. The growth rate decays smoothly until the growth multiplier ϑ^{g} has reached its maximum value $\vartheta^{\max}$, here shown for $\gamma = 2.0$ and $\tau = 1.0$ (left). The nonlinearity of the growth process increases for increasing γ, here shown for $\vartheta^{\max} = 2.5$ and $\tau = 1.0$, (right).

Remark 2 (*Dissipation*). In the present approach, we characterize the growth process through a single growing solid phase and essentially neglect the biochemical origin of the growing material. To phenomenologically account for the interaction with other species, we have introduced the extra term $\mathcal{S}_0$ in the dissipation inequality (7), which could otherwise be violated, in particular in the context of material strengthening (Kuhl and Steinmann, 2003a, 2003b). This extra term gains an illustrative biochemical interpretation in the context of mixture theories (Garikipati et al., 2004; Humphrey and Rajagopal, 2002; Klisch et al., 2003).

Remark 3 (*Rotation*). Apart from the theory of finite crystal plasticity, kinematic approaches to the finite inelasticity of non-crystalline materials are frequently based on the multiplicative decomposition of the deformation gradient. In contrast to the former, where the multiplicative decomposition has a clear geometric interpretation, the latter kinematic settings require an additional assumption regarding the symmetry of the elastic part of the deformation gradient or the plastic spin due to the non-uniqueness of rotation (Boyce et al., 1989; Naghdi, 1990; Xiao et al., 2006). In the present kinematic formulation of growth, the symmetric growth tensor $\boldsymbol{F}^{\mathrm{g}}$ (12) is motivated by the underlying architecture of the heart, which has a well-defined orthotropic structure, see Fig. 1. As a consequence, the rotation is lumped into the elastic part of the deformation gradient, and the plastic spin in the fictitious intermediate configuration vanishes identically. This is in accordance with common practice in the literature (Boyce et al., 1989).

3. Discrete equations of finite growth

Since the governing equations for finite growth are complex and highly nonlinear, it is virtually impossible to find analytical solutions. To solve the governing equations for finite growth numerically on a local level, we propose a finite difference scheme to discretize the evolution equations for the growth multipliers (13) in time. To solve the overall equations numerically on a global level, we propose the finite element method to discretize the equations for finite growth (1), (6) and (10) in space. In this section, we first derive the discrete residual and the corresponding tangent moduli for the local Newton iteration to iteratively determine the growth multipliers ϑ^{g}. Then, we derive the stress expression and the constitutive moduli which enter the discrete residual and the corresponding tangent of the global Newton iteration.

3.1. Local Newton iteration—iterative update of growth variables

Our goal is to solve the evolution equations for the growth multipliers (13) to determine the current set of growth multipliers ϑ^{g} for a given current deformation state $\boldsymbol{F}$ at the current time t, and given growth multipliers $\vartheta^{\mathrm{g}}_{\mathrm{n}}$ at the end of the previous time step t_{n}. We introduce the following finite difference approximation of the first order material time derivative,

$$\dot{\vartheta}^{\mathrm{g}} = \frac{1}{\Delta t}[\vartheta^{\mathrm{g}} - \vartheta^{\mathrm{g}}_{\mathrm{n}}], \tag{14}$$

where $\Delta t := t - t_{\mathrm{n}} > 0$ denotes the actual time increment. In the spirit of implicit time stepping schemes, we now reformulate the generic evolution equations (13) with the help of the finite difference approximation (14) introducing the discrete residual R in terms of the unknown growth multipliers ϑ^{g}.

$$\mathsf{R} = \vartheta^{\mathrm{g}} - \vartheta^{\mathrm{g}}_{\mathrm{n}} - \boldsymbol{k}^{\mathrm{g}} \cdot \boldsymbol{\phi}^{\mathrm{g}} \Delta t \doteq 0. \tag{15}$$

Its linearization renders the local tangent moduli for local Newton iteration,

$$\mathsf{K} = \frac{\partial \mathsf{R}}{\partial \vartheta^{\mathrm{g}}} = \boldsymbol{I} - \left[\boldsymbol{k}^{\mathrm{g}} \cdot \frac{\partial \boldsymbol{\phi}^{\mathrm{g}}}{\partial \vartheta^{\mathrm{g}}} + \boldsymbol{\phi}^{\mathrm{g}} \cdot \frac{\partial \boldsymbol{k}^{\mathrm{gt}}}{\partial \vartheta^{\mathrm{g}}} \right] \Delta t, \tag{16}$$

which define the iterative update $\vartheta^{\mathrm{g}} \leftarrow \vartheta^{\mathrm{g}} - \mathsf{K}^{-1} \cdot \mathsf{R}$ of the growth multipliers. Recall that in the simplified case of only one growth multiplier ϑ^{g}, both the residual R and the tangent K are scalar-valued.

3.2. Global Newton iteration—consistent linearization of finite growth

Once we have iteratively determined the set of growth multipliers ϑ^{g} for the given deformation state $\boldsymbol{F}$ and the given history $\vartheta^{\mathrm{g}}_{\mathrm{n}}$, we can successively determine the growth tensor $\boldsymbol{F}^{\mathrm{g}}$ from Eq. (12), the elastic tensor $\boldsymbol{F}^{\mathrm{e}} = \boldsymbol{F} \cdot \boldsymbol{F}^{\mathrm{g}-1}$ from Eq. (1), the elastic stress $\boldsymbol{S}^{\mathrm{e}}$ from Eq. (10), and lastly, the second Piola Kirchhoff stress $\boldsymbol{S}$

$$\boldsymbol{S} = 2\frac{\partial \psi}{\partial \boldsymbol{C}} = 2\frac{\partial \psi}{\partial \boldsymbol{C}^{\mathrm{e}}} : \frac{\partial \boldsymbol{C}^{\mathrm{e}}}{\partial \boldsymbol{C}} = \boldsymbol{F}^{\mathrm{g}-1} \cdot 2\frac{\partial \psi}{\partial \boldsymbol{C}^{\mathrm{e}}} \cdot \boldsymbol{F}^{\mathrm{g}-\mathrm{t}} = \boldsymbol{F}^{\mathrm{g}-1} \cdot \boldsymbol{S}^{\mathrm{e}} \cdot \boldsymbol{F}^{\mathrm{g}-\mathrm{t}} \tag{17}$$

which enters the equilibrium equation (6), or in the notion of the finite element method, the global discrete residual. Its linearization with respect to the total right Cauchy Green tensor renders the Lagrangian constitutive moduli L which are

essential for the global Newton iteration.

$$\mathbf{L} = 2\frac{\mathrm{d}\boldsymbol{S}(\boldsymbol{F},\boldsymbol{F}^{\mathrm{g}})}{\mathrm{d}\boldsymbol{C}} = 2\frac{\partial \boldsymbol{S}}{\partial \boldsymbol{C}}\bigg|_{\boldsymbol{F}^{\mathrm{g}}} + 2\left[\frac{\partial \boldsymbol{S}}{\partial \boldsymbol{F}^{\mathrm{g}}} : \frac{\partial \boldsymbol{F}^{\mathrm{g}}}{\partial \vartheta^{\mathrm{g}}}\right] \otimes \frac{\partial \vartheta^{\mathrm{g}}}{\partial \boldsymbol{C}}\bigg|_{\boldsymbol{F}}. \tag{18}$$

The constitutive moduli take a characteristic structure consisting of four terms. While the first two terms are generic, the third and fourth terms depend on the choice of the growth tensor (12) and on the choice of the evolution equation (13), respectively. The first term $2\partial \boldsymbol{S}/\partial \boldsymbol{C}$ is nothing but the pull back of the elastic moduli $\mathbf{L}^{\mathrm{e}}$ onto the reference configuration,

$$2\frac{\partial \boldsymbol{S}}{\partial \boldsymbol{C}} = 2\frac{\partial[\boldsymbol{F}^{\mathrm{g}-1}\cdot\boldsymbol{S}^{\mathrm{e}}\cdot\boldsymbol{F}^{\mathrm{g}-\mathrm{t}}]}{\partial \boldsymbol{C}} = [\boldsymbol{F}^{\mathrm{g}-1}\overline{\otimes}\boldsymbol{F}^{\mathrm{g}-1}] : \mathbf{L}^{\mathrm{e}} : [\boldsymbol{F}^{\mathrm{g}-\mathrm{t}}\overline{\otimes}\boldsymbol{F}^{\mathrm{g}-\mathrm{t}}], \tag{19}$$

where $\mathbf{L}^{\mathrm{e}} = 2\partial \boldsymbol{S}^{\mathrm{e}}/\partial \boldsymbol{C}^{\mathrm{e}}$ are the constitutive moduli of the elastic material model as introduced in Eq. (11). The second term $\partial \boldsymbol{S}/\partial \boldsymbol{F}^{\mathrm{g}}$ consists of two contributions that resemble a geometric and a material stiffness contribution known from nonlinear continuum mechanics:

$$\frac{\partial \boldsymbol{S}}{\partial \boldsymbol{F}^{\mathrm{g}}} = \frac{\partial[\boldsymbol{F}^{\mathrm{g}-1}\cdot\boldsymbol{S}^{\mathrm{e}}\cdot\boldsymbol{F}^{\mathrm{g}-\mathrm{t}}]}{\partial \boldsymbol{F}^{\mathrm{g}}} = -[\boldsymbol{F}^{\mathrm{g}-1}\overline{\otimes}\boldsymbol{S} + \boldsymbol{S}\underline{\otimes}\boldsymbol{F}^{\mathrm{g}-1}] - [\boldsymbol{F}^{\mathrm{g}-1}\overline{\otimes}\boldsymbol{F}^{\mathrm{g}-1}] : \frac{1}{2}\mathbf{L}^{\mathrm{e}} : [\boldsymbol{F}^{\mathrm{g}-\mathrm{t}}\underline{\otimes}\boldsymbol{C}^{\mathrm{e}} + \boldsymbol{C}^{\mathrm{e}}\overline{\otimes}\boldsymbol{F}^{\mathrm{g}-\mathrm{t}}]. \tag{20}$$

The third term $\partial \boldsymbol{F}^{\mathrm{g}}/\partial \vartheta^{\mathrm{g}}$ and the fourth term $\partial \vartheta^{\mathrm{g}}/\partial \boldsymbol{C}$ depend on the particular choice for the growth tensor $\boldsymbol{F}^{\mathrm{g}}$ and on the evolution equation for the growth multipliers ϑ^{g}, respectively. Particular formats will be specified in the example Sections 5–7.

Remark 4 (*Non-symmetry*). From Eq. (18), we can conclude that the generic growth formulation is in general non-symmetric. Only for very special cases, in which growth is driven by its thermodynamically conjugate force, the constitutive moduli, and, accordingly, the entire global iteration matrix, turn out to be symmetric:

Remark 5 (*Push forward*). Most finite strain based finite element programs are formulated in a spatial setting and require the calculation of the Kirchhoff stresses

$$\boldsymbol{\tau} = \boldsymbol{F}\cdot\boldsymbol{S}\cdot\boldsymbol{F}^{\mathrm{t}} \tag{21}$$

and the Kirchhoff moduli

$$\mathbf{e} = [\boldsymbol{F}\overline{\otimes}\boldsymbol{F}] : \mathbf{L} : [\boldsymbol{F}^{\mathrm{t}}\overline{\otimes}\boldsymbol{F}^{\mathrm{t}}] \tag{22}$$

which can be obtained through a straightforward push forward with the total deformation gradient $\boldsymbol{F}$.

4. Generic biventricular heart model: discretization, boundary conditions, and loads

Before we illustrate the features of the proposed algorithmic framework for stress-driven isotropic growth in Section 5, strain-driven transversely isotropic growth in Section 6, and stress-driven transversely isotropic growth in Section 7, we will briefly introduce the generic biventricular heart model (Göktepe et al., 2010b), that we will use to compare all three algorithms. In this prototype model illustrated in Fig. 6, left, the left and right ventricles, the lower chambers of the heart, are represented through two truncated ellipsoids with heights of 70 and 60 mm, and radii of 30 and 51 mm, respectively, connected such that the right ventricle blends smoothly into the left ventricle from apex to base. The left ventricle which pumps oxygenated blood into the body operates at a higher pressure and typically has a larger wall thickness than the

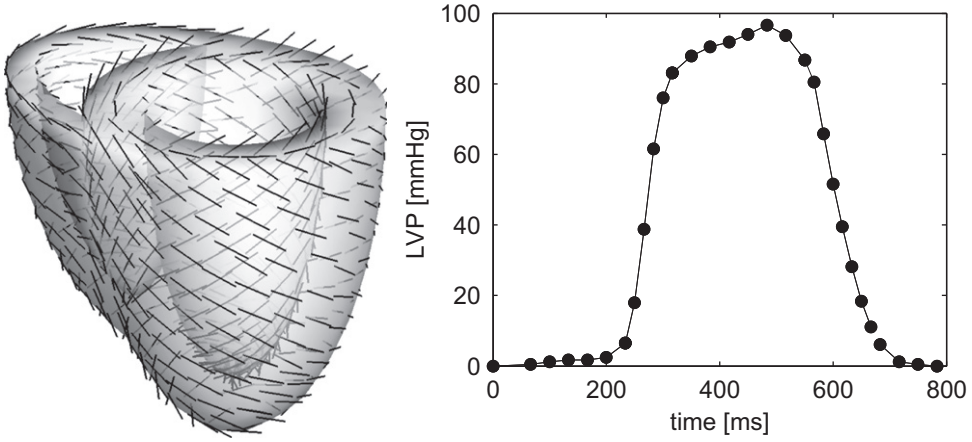

Fig. 6. Generic biventricular heart model generated from two truncated ellipsoids (Göktepe et al., 2010b), with heights of 70 and 60 mm, radii of 30 and 51 mm, and wall thicknesses of 12 and 6 mm, respectively (left). The left ventricle is subjected to cycles of the experimentally measured left ventricular pressure (Göktepe et al., 2010c), while one-fifth of this pressure is applied to the right ventricle (right).

right ventricle which pumps deoxygenated blood into the lungs. We therefore assume an initial left ventricular wall thickness of 12 mm while the right ventricular wall is assumed to be 6 mm thick. The left ventricular endocardium is subjected to cycles of the experimentally measured left ventricular pressure illustrated in Fig. 4, right (Göktepe et al., 2010c). One-fifth of this pressure is applied to the right ventricular endocardium. For the lack of better knowledge, we apply homogeneous Dirichlet boundary conditions to all nodes on the basal plane. In addition, to mimic the boundary conditions imposed by the surrounding tissue, we support all nodes of the epicardium by linear springs with a stiffness of $k=10^{-3}$ N/mm both in the radial and tangential directions. The generic biventricular heart model is discretized with 3910 linear tetrahedral elements connected at 1028 nodes. In the healthy heart, cardiomyocytes are arranged helically around the ventricles. Here, we assume that the fiber directions $\boldsymbol{f}_0$ vary transmurally from an inclination of -55° in the epicardium, the outer wall, to $+55^\circ$ in the endocardium, the inner wall, measured with respect to the basal plane. The fiber angle is assumed to decay gradually from base to apex towards a final value of 0°, see Fig. 6, left. For the sake of simplicity, the myocardial sheet directions $\boldsymbol{s}_0$ are assumed to be oriented normal to the endocardium and epicardium. Following the literature (Himpel et al., 2005; Menzel, 2005), the material parameters for the baseline elastic response are chosen to $\lambda = 0.577$ MPa and $\mu = 0.385$ MPa. However, the extension of the model to a more physiological orthotropic baseline elasticity along the fiber, sheet, and sheet plane normal directions is straightforward and part of current research activities (Göktepe et al., 2010b; Holzapfel and Ogden, 2009). At this point, the choice of the time parameter $\tau = 3.2$ MPa s and the nonlinearity parameter $\gamma = 2.0$ are relatively generic since they only affect the speed of growth, but not the end result, see Fig. 5. In the future, however, we will use these two parameters to calibrate our model against clinical observations. All the above features will be the basis for the examples in Sections 5.4, 6.4, and 7.4, to allow for a direct comparison of the three different growth models.

5. Example athletic heart: stress-driven isotropic growth

5.1. Physiology of athlete's heart

Athlete's heart syndrome, also commonly known as athlete's heart, is a medical condition in which the heart grows beyond its normal size due to a significant amount of exercise (Sedehi and Ashley, 2010). The enlargement of the heart reflects a physiological adaptation in response to both elevated pressure and increased filling. A typical example is the cardiac output of high performance athletes, which may increase from approximately 6 l/min at rest to 40 l/min during exercise (Ekblom and Hermansen, 1968). On the microscopic scale, training has been reported to significantly affect cardiomyocyte size with an increase of up to 40% (Garciarena et al., 2009). It is typically associated with a proportional increase in cardiomyocyte length and width (Hunter and Chien, 1999). On the macroscopic scale, these cellular changes manifest themselves in an increase in cardiac mass of up to 50% (Pluim et al., 2000). Pressure overload triggers ventricular wall thickening, with reported posterior wall thickening from 8.8 to 10.3 mm in endurance training and to 11.0 mm in strength training. Volume overload on the contrary, induces an enlargement of the heart with a reported increase of the left ventricular end diastolic inner diameter from 49.6 to 52.1 mm in strength training and to 53.7 mm in endurance training (Pluim et al., 2000). These studies support the hypothesis that strength training such as weight lifting preliminary triggers concentric left ventricular hypertrophy, i.e., heart muscle thickening, to withstand higher stress levels, whereas endurance training such as cycling primarily triggers eccentric left ventricular hypertrophy, i.e., cavity growth, to increase cardiac output (Mihl et al., 2008). Fortunately, the adaptive cardiac changes stimulated by frequent training are typically reversible and the features of the athlete heart usually decrease upon detraining.

5.2. Governing equations athlete's heart

In what follows, we model the effects of combined endurance and strength training, i.e., the proportional increase in cardiomyocyte length and width, resulting in a combined thickening of the left ventricular wall and an increasing chamber size, common to many high performance athletes (Hunter and Chien, 1999; Pluim et al., 2000). Accordingly, we characterize the athlete's heart through a pressure-driven, isotropic, volumetric, reversible growth process, introducing one single growth multiplier ϑ^{g},

$$\vartheta^{\mathrm{f}} = \vartheta^{\mathrm{s}} = \vartheta^{\mathrm{n}} = \vartheta^{\mathrm{g}} \tag{23}$$

such that the growth tensor is purely volumetric and can be expressed as a scaled unit tensor $\boldsymbol{I}$:

$$\boldsymbol{F}^{\mathrm{g}} = \vartheta^{\mathrm{g}}\boldsymbol{I}. \tag{24}$$

This simplified assumption introduces an explicit expression for the inverse growth tensor $\boldsymbol{F}^{\mathrm{g}-1}$,

$$\boldsymbol{F}^{\mathrm{g}-1} = \frac{1}{\vartheta^{\mathrm{g}}}\boldsymbol{I} \tag{25}$$

and for the derivative of growth $\partial \boldsymbol{F}^{\mathrm{g}}/\partial \vartheta^{\mathrm{g}}$ in terms of the unity tensor,

$$\frac{\partial \boldsymbol{F}^{\mathrm{g}}}{\partial \vartheta^{\mathrm{g}}} = \boldsymbol{I}, \tag{26}$$

which will later allow a significant simplification of the discrete stress (17) and constitutive moduli (18). We shall assume that growth of athlete's hearts is primarily stress-driven, introducing the following specification of the evolution equation (13):

$$\dot{\vartheta}^{\mathrm{g}} = k^{\mathrm{g}}(\vartheta^{\mathrm{g}})\phi^{\mathrm{g}}(\boldsymbol{M}^{\mathrm{e}}). \tag{27}$$

The growth process is scaled by a function k^{g} that prevents unbounded growth (Lubarda and Hoger, 2002):

$$k^{\mathrm{g}} = \frac{1}{\tau}\left[\frac{\vartheta^{\max}-\vartheta^{\mathrm{g}}}{\vartheta^{\max}-1}\right]^{\gamma} \quad \text{with} \quad \frac{\partial k^{\mathrm{g}}}{\partial \vartheta^{\mathrm{g}}} = -\frac{\gamma}{[\vartheta^{\max}-\vartheta^{\mathrm{g}}]}k^{\mathrm{g}}. \tag{28}$$

Motivated by thermodynamic considerations (Himpel et al., 2005), growth is driven by the trace of the Mandel stress $\boldsymbol{M}^{\mathrm{e}} = \boldsymbol{C}^{\mathrm{e}} \cdot \boldsymbol{S}^{\mathrm{e}}$ which reflects the ventricular pressure. Growth is activated once the ventricular pressure during physical activity exceeds the physiological threshold level $M^{\mathrm{e\ crit}}$:

$$\phi^{\mathrm{g}} = \mathrm{tr}(\boldsymbol{M}^{\mathrm{e}}) - M^{\mathrm{e\ crit}} \quad \text{with} \quad \frac{\partial \phi^{\mathrm{g}}}{\partial \vartheta^{\mathrm{g}}} = -\frac{1}{\vartheta^{\mathrm{g}}}[2\,\mathrm{tr}(\boldsymbol{M}^{\mathrm{e}}) + \boldsymbol{C}^{\mathrm{e}} : \mathsf{L}^{\mathrm{e}} : \boldsymbol{C}^{\mathrm{e}}]. \tag{29}$$

As proposed in Section 3.1, we apply an unconditionally stable implicit Euler backward scheme with $\dot{\vartheta}^{\mathrm{g}} = [\vartheta^{\mathrm{g}} - \vartheta^{\mathrm{g}}_{\mathrm{n}}]/\Delta t$, to specify the discrete residual introduced in Eq. (15):

$$\mathsf{R} = \vartheta^{\mathrm{g}} - \vartheta^{\mathrm{g}}_{\mathrm{n}} - \frac{1}{\tau}\left[\frac{\vartheta^{\max}-\vartheta^{\mathrm{g}}}{\vartheta^{\max}-1}\right]^{\gamma}[\mathrm{tr}(\boldsymbol{M}^{\mathrm{e}}) - M^{\mathrm{ecrit}}]\Delta t \doteq 0. \tag{30}$$

Its linearization renders the tangent moduli for local Newton iteration as introduced in Eq. (16):

$$\mathsf{K} = \frac{\partial \mathsf{R}}{\partial \vartheta^{\mathrm{g}}} = 1 - \left[k^{\mathrm{g}}\frac{\partial \phi^{\mathrm{g}}}{\partial \vartheta^{\mathrm{g}}} + \phi^{\mathrm{g}}\frac{\partial k^{\mathrm{g}}}{\partial \vartheta^{\mathrm{g}}}\right]\Delta t \tag{31}$$

to iteratively update the isotropic growth multiplier $\vartheta^{\mathrm{g}} \leftarrow \vartheta^{\mathrm{g}} - \mathsf{R}/\mathsf{K}$. Having determined the growth multiplier ϑ^{g}, we can calculate the growth tensor $\boldsymbol{F}^{\mathrm{g}} = \vartheta^{\mathrm{g}}\boldsymbol{I}$ and the elastic tensor $\boldsymbol{F}^{\mathrm{e}} = \vartheta^{\mathrm{g}-1}\boldsymbol{F}$ to determine the elastic stress $\boldsymbol{S}^{\mathrm{e}}$ and the total second Piola Kirchhoff stress $\boldsymbol{S}$ from Eq. (17), which takes the following simple representation:

$$\boldsymbol{S} = \frac{1}{\vartheta^{\mathrm{g}2}}\boldsymbol{S}^{\mathrm{e}}. \tag{32}$$

To determine the overall constitutive moduli of isotropic growth, we can then evaluate the generic constitutive moduli from Eq. (18), with the second and third term collectively given as follows:

$$\frac{\partial \boldsymbol{S}}{\partial \vartheta^{\mathrm{g}}} = \frac{\partial \boldsymbol{S}}{\partial \boldsymbol{F}^{\mathrm{g}}} : \frac{\partial \boldsymbol{F}^{\mathrm{g}}}{\partial \vartheta^{\mathrm{g}}} = -\frac{2}{\vartheta^{\mathrm{g}3}}\left[\boldsymbol{S}^{\mathrm{e}} + \frac{1}{2}\mathsf{L}^{\mathrm{e}} : \boldsymbol{C}^{\mathrm{e}}\right] \tag{33}$$

and the fourth term taking the following expression:

$$\frac{\partial \vartheta^{\mathrm{g}}}{\partial \boldsymbol{C}} = \frac{\partial \vartheta^{\mathrm{g}}}{\partial \boldsymbol{C}^{\mathrm{e}}} : \frac{\partial \boldsymbol{C}^{\mathrm{e}}}{\partial \boldsymbol{C}} = \frac{1}{\vartheta^{\mathrm{g}2}}\left[\frac{k^{\mathrm{g}}}{\mathsf{K}}\Delta t\right]\left[\frac{1}{2}\boldsymbol{C}^{\mathrm{e}} : \mathsf{L}^{\mathrm{e}} + \boldsymbol{S}^{\mathrm{e}}\right]. \tag{34}$$

Summarizing all terms of Eq. (18), with (19), (33), and (34) we obtain the remarkably simple Lagrangian constitutive moduli for isotropic pressure-driven growth:

$$\mathsf{L} = \frac{1}{\vartheta^{\mathrm{g}4}}\mathsf{L}^{\mathrm{e}} - \frac{4}{\vartheta^{\mathrm{g}5}}\frac{k^{\mathrm{g}}}{\mathsf{K}}\Delta t\left[\boldsymbol{S}^{\mathrm{e}} + \frac{1}{2}\mathsf{L}^{\mathrm{e}} : \boldsymbol{C}^{\mathrm{e}}\right] \otimes \left[\frac{1}{2}\boldsymbol{C}^{\mathrm{e}} : \mathsf{L}^{\mathrm{e}} + \boldsymbol{S}^{\mathrm{e}}\right]. \tag{35}$$

Remark 6 (*Symmetry for isotropic growth*). Although the constitutive moduli $\boldsymbol{L} = 2\,\mathrm{d}\boldsymbol{S}/\mathrm{d}\boldsymbol{C}$ of finite growth can in general be non-symmetric, for the case of Mandel stress-driven isotropic growth discussed here, the overall tangent moduli given in Eq. (35) turn out to be symmetric. Symmetry holds, since we have suggested a growth criterion $\phi^{\mathrm{g}} = \mathrm{tr}(\boldsymbol{M}^{\mathrm{e}}) - M^{\mathrm{ecrit}}$ in terms of the Mandel stress of the intermediate configuration $\boldsymbol{M}^{\mathrm{e}} = \boldsymbol{C}^{\mathrm{e}} \cdot \boldsymbol{S}^{\mathrm{e}}$, i.e., the thermodynamically conjugate variable to the growth velocity gradient $\boldsymbol{L}^{\mathrm{g}} = \dot{\boldsymbol{F}}^{\mathrm{g}} \cdot \boldsymbol{F}^{\mathrm{g}-1}$, as the driving force for growth.

Remark 7 (*Simplified push forward for isotropic growth*). In case the finite element program requires the calculation of the Kirchhoff stress

$$\boldsymbol{\tau} = \boldsymbol{F} \cdot \boldsymbol{S} \cdot \boldsymbol{F}^{\mathrm{t}} = \boldsymbol{F}^{\mathrm{e}} \cdot \boldsymbol{S}^{\mathrm{e}} \cdot \boldsymbol{F}^{\mathrm{et}} = \vartheta^{\mathrm{g}2}\boldsymbol{F}^{\mathrm{e}} \cdot \boldsymbol{S} \cdot \boldsymbol{F}^{\mathrm{et}} \tag{36}$$

and the Kirchhoff moduli

$$\mathsf{e} = [\boldsymbol{F} \overline{\otimes} \boldsymbol{F}] : \mathsf{L} : [\boldsymbol{F}^{\mathrm{t}} \overline{\otimes} \boldsymbol{F}^{\mathrm{t}}] = \vartheta^{\mathrm{g}4}[\boldsymbol{F}^{\mathrm{e}} \overline{\otimes} \boldsymbol{F}^{\mathrm{e}}] : \mathsf{L} : [\boldsymbol{F}^{\mathrm{et}} \overline{\otimes} \boldsymbol{F}^{\mathrm{et}}] \tag{37}$$

we can perform push forward operations which take a simplified format in the isotropic case through a simple scaling with the growth multiplier ϑ^{g}.

Table 1
Algorithmic treatment of stress-driven isotropic growth.

given $\boldsymbol{F}$ and $\vartheta^{\mathrm{g}}_{\mathrm{n}}$	
initialize $\vartheta^{\mathrm{g}} \leftarrow \vartheta^{\mathrm{g}}_{\mathrm{n}}$	
local Newton iteration	
calculate elastic tensor $\boldsymbol{F}^{\mathrm{e}} = \boldsymbol{F}/\vartheta^{\mathrm{g}}$	(1)
calculate elastic right Cauchy Green tensor $\boldsymbol{C}^{\mathrm{e}} = \boldsymbol{F}^{\mathrm{et}} \cdot \boldsymbol{F}^{\mathrm{e}}$	(2)
calculate second Piola Kirchhoff stress $\boldsymbol{S}^{\mathrm{e}} = 2\partial\psi/\partial\boldsymbol{C}^{\mathrm{e}}$	(10)
check growth criterion $\phi^{\mathrm{g}} = \mathrm{tr}(\boldsymbol{C}^{\mathrm{e}} \cdot \boldsymbol{S}^{\mathrm{e}}) - M^{\mathrm{ecrit}} \geq 0$?	(29)
calculate growth function $k^{\mathrm{g}} = [[\vartheta^{\max} - \vartheta^{\mathrm{g}}]/[\vartheta^{\max} - 1]]^{\gamma}/\tau$	(28)
calculate residual $\mathsf{R} = \vartheta^{\mathrm{g}} - \vartheta^{\mathrm{g}}_{\mathrm{n}} - k^{\mathrm{g}}\phi^{\mathrm{g}}\Delta t$	(30)
calculate tangent $\mathsf{K} = \partial\mathsf{R}/\partial\vartheta^{\mathrm{g}}$	(31)
update growth multiplier $\vartheta^{\mathrm{g}} \leftarrow \vartheta^{\mathrm{g}} - \mathsf{R}/\mathsf{K}$	
check convergence $\mathsf{R} \leq \mathrm{tol}$?	
calculate second Piola Kirchhoff stress $\boldsymbol{S} = 1/\vartheta^{\mathrm{g}2}\boldsymbol{S}^{\mathrm{e}}$	(32)
calculate Lagrangian moduli L	(35)
push forward to Kirchhoff stresses $\boldsymbol{\tau} = \boldsymbol{F} \cdot \boldsymbol{S} \cdot \boldsymbol{F}^{\mathrm{t}}$	(36)
push forward to Eulerian moduli $\mathsf{e} = [\boldsymbol{F} \overline{\otimes} \boldsymbol{F}] : \mathsf{L} : [\boldsymbol{F}^{\mathrm{t}} \overline{\otimes} \boldsymbol{F}^{\mathrm{t}}]$	(37)

5.3. Algorithmic treatment of athlete's heart

Table 1 illustrates the algorithmic flowchart for stress-driven isotropic growth. Remarkably, throughout the entire algorithm, we never have to calculate or store the growth tensor $\boldsymbol{F}^{\mathrm{g}}$. Instead, the algorithm manifests itself in a simple scalar scaling with $1/\vartheta^{\mathrm{g}}$ and is therefore extremely straightforward and easy to implement. Recall that in our model, the growth process is driven by the Mandel stress, such that the overall constitutive moduli for isotropic growth are symmetric and a symmetric finite element solver can be applied.

5.4. Example of athlete's heart

To simulate stress-driven isotropic growth using the model illustrated in Section 4, we have to specify two additional growth parameters, the physiological pressure threshold $M^{\mathrm{e\ crit}} = 0.012$ MPa and the maximum growth threshold $\vartheta^{\max} = 1.75$. Fig. 7 documents the result of our simulation of stress-driven isotropic growth. The illustrated time sequence displays the deformed configuration at end systole for four consecutive load cycles. Characteristic for athlete's heart, isotropic growth manifests itself in left ventricular dilation together with left ventricular wall thickening. The isotropic growth multiplier ϑ gradually increases from its baseline value $\vartheta = 1.00$ to its maximum value $\vartheta^{\max} = 1.75$ in response to elevated pressures. The growth process is activated when the driving force, the trace of the Mandel stress $\mathrm{tr}(\boldsymbol{M}^{\mathrm{e}})$, locally exceeds the critical physiological threshold $M^{\mathrm{e\ crit}} = 0.012$ MPa. During cyclic loading with the pressure function shown in Fig. 6, the growth process is only activated at peak pressures during systole, while it is dormant at low pressures during diastole. On the macroscopic scale, the athlete's heart manifests itself in a progressive apical growth with a considerably increase in left ventricular cavity size to enable increased cardiac output during exercise. To withstand higher blood pressure levels during training, the heart muscle grows and the wall becomes thicker. Although there is a general agreement in the literature that endurance training is associated with elevated filling volumes which trigger cardiac dilation to increase cardiac output, while strength training is associated with elevated pressures which trigger ventricular wall thickening to withstand higher stress levels, high performance training typically stimulates both forms of physiological growth (Hunter and Chien, 1999; Maron and Pelliccia, 2006; Sedehi and Ashley, 2010). Accordingly, in our simulation, both ventricular dilation and wall thickening appeared simultaneously characterized through an isotropic cardiomyocyte growth. As such, the simulation documented in Fig. 7 is excellent qualitative agreement with the physiological characteristics of athlete's heart summarized in Section 5.1: (i) physiological adaptation of the ventricular volume and (ii) physiological adaptation of the wall thickness.

6. Example cardiac dilation: strain-driven transversely isotropic growth

6.1. Pathophysiology of cardiac dilation

Cardiac dilation is a chronic medical condition in which the pumping efficiency of the heart may be gradually reduced as the heart becomes progressively enlarged and successively weaker. It is amongst the most common causes of heart failure with less than 50% survival after 10 years. A typical cause of dilated cardiac growth is myocardial infarction, after which the infarcted ventricle might dilate in response to volume overload in an attempt to maintain cardiac output at a physiological level (Cheng et al., 2006). Maladaptive ventricular dilation can be the origin of further unfavorable pathologies such as functional mitral regurgitation, a condition in which the valves of the heart tend to leak because of

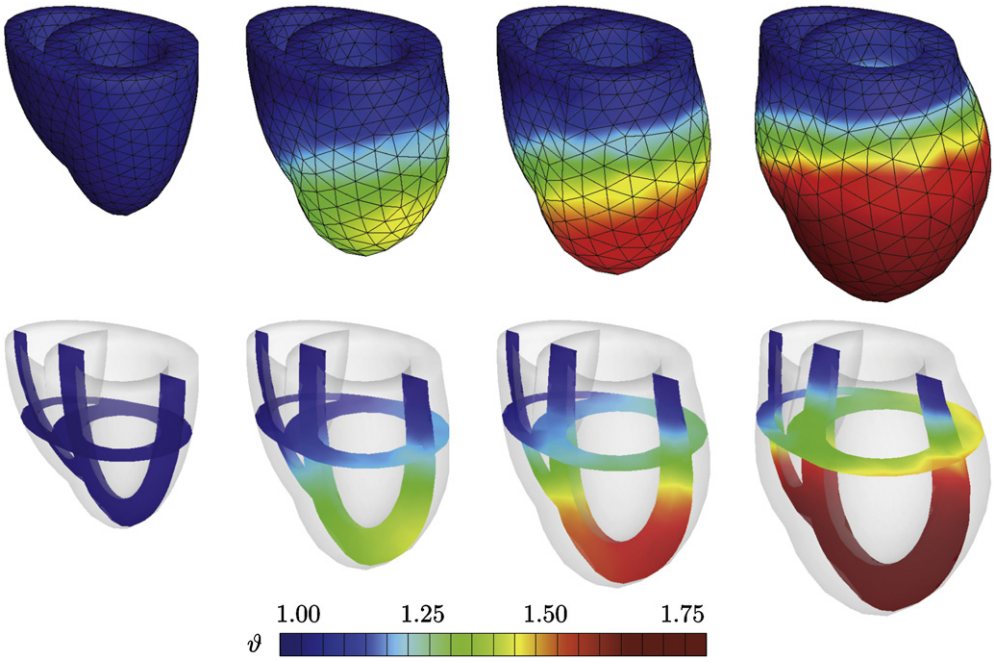

Fig. 7. Athlete's heart, stress-driven isotropic eccentric and concentric growth, left ventricular dilation and wall thickening. The isotropic growth multiplier ϑ gradually increases from 1.00 to 1.75 as the individual cardiomyocytes grow both eccentrically and concentrically. On the macroscopic scale, the athlete's heart manifests itself in a progressive apical growth with a considerably increase in left ventricular cavity size to enable increased cardiac output during exercise. To withstand higher blood pressure levels during training, the heart muscle grows and the wall thickens.

chronic changes in cardiac geometry (Göktepe et al., 2010c). On the microscopic scale, volume overload triggers the assembly of new sarcomeres which are deposited in series with the existing sacromeres units. This causes the cardiomyocytes to lengthen (Kumar et al., 2005). On the macroscopic scale, these maladaptive alterations of cardiomyocyte shape manifests themselves in the dilation of the left ventricle, a change in ventricular shape from elliptical to spherical (Cheng et al., 2006), and a decrease in ejection fraction (Berne and Levy, 2001), while the wall thickness typically remains unaltered, see Fig. 8. The mass of the heart, however, may increase drastically up to 1000 g, which is about three times the weight of a normal heart (Kumar et al., 2005). This pathological adaptation of the heart muscle is usually progressive and there is an ongoing debate to which extend it may be reversible.

6.2. Governing equations of cardiac dilation

In our continuum growth model, we represent cardiac dilation as a strain-driven, transversely isotropic, irreversible growth process. It is characterized through one single growth multiplier ϑ^{g} that reflects serial sarcomere deposition and induces an irreversible cardiomyocyte stretch along the cell's long axis $\boldsymbol{f}_0$:

$$\vartheta^{\mathrm{f}}=\vartheta^{\mathrm{g}} \quad \text{and} \quad \vartheta^{\mathrm{s}}=\vartheta^{\mathrm{n}}=1. \tag{38}$$

In cardiac dilation, growth is actually one dimensional, and the total cardiomyocyte stretch $\lambda=\sqrt{\boldsymbol{f}_0\cdot\boldsymbol{F}^{\mathrm{t}}\cdot\boldsymbol{F}\cdot\boldsymbol{f}_0}$ obeys a multiplicative decomposition similar to the deformation gradient itself. It can thus be expressed as the product of the elastic stretch λ^{e}, i.e., the healthy cardiomyocyte stretch during diastole, and the growth stretch $\lambda^{\mathrm{g}}=\vartheta^{\mathrm{g}}$, i.e., the pathological cardiomyocyte stretch during eccentric growth,

$$\lambda=\lambda^{\mathrm{e}}\lambda^{\mathrm{g}}, \tag{39}$$

whereby the latter is identical to the growth multiplier:

$$\lambda^{\mathrm{g}}=\vartheta^{\mathrm{g}}. \tag{40}$$

The growth tensor $\boldsymbol{F}^{\mathrm{g}}$ can thus be expressed exclusively in terms of the eccentric cardiomyocyte stretch λ^{g}

$$\boldsymbol{F}^{\mathrm{g}}=\boldsymbol{I}+[\lambda^{\mathrm{g}}-1]\boldsymbol{f}_0\otimes\boldsymbol{f}_0 \tag{41}$$

and its inverse can be given explicitly using the Sherman–Morrison formula:

$$\boldsymbol{F}^{\mathrm{g}-1}=\boldsymbol{I}-\frac{\lambda^{\mathrm{g}}-1}{\lambda^{\mathrm{g}}}\boldsymbol{f}_0\otimes\boldsymbol{f}_0. \tag{42}$$

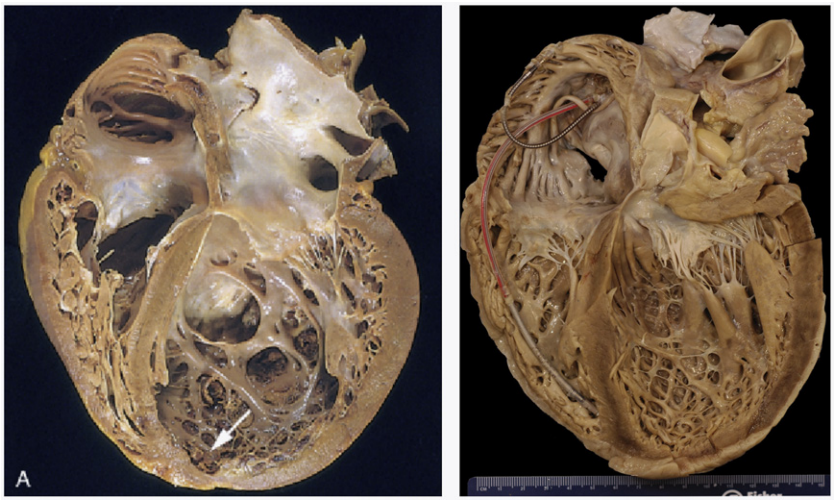

Fig. 8. Cardiac dilation, strain-driven eccentric growth, and increase in cavity size at constant wall thickness. The heart is usually enlarged, rounded, flabby, and heavy with a weight of up to three times its normal weight (left), reprinted with permission from Kumar et al. (2005). Heart specimen from a patient with cardiac dilation who died in end-stage heart failure. The ventricles are significantly dilated while the wall thickness has remained unaltered, courtesy of Allen P. Burke.

Its derivative with respect to the growth multiplier which defines the third term for the constitutive moduli in Eq. (18), takes the following simple representation:

$$\frac{\partial \boldsymbol{F}^{\mathrm{g}}}{\partial \vartheta^{\mathrm{g}}} = \boldsymbol{f}_0 \otimes \boldsymbol{f}_0 . \tag{43}$$

Motivated by physiological observations of volume overload induced dilation, we introduce a strain-driven evolution law for the pathological cardiomyocyte stretch λ^{g}:

$$\dot{\lambda}^{\mathrm{g}} = k^{\mathrm{g}}(\lambda^{\mathrm{g}})\phi^{\mathrm{g}}(\lambda^{\mathrm{e}}). \tag{44}$$

It is based on a weighting function k^{g}

$$k^{\mathrm{g}} = \frac{1}{\tau}\left[\frac{\lambda^{\max}-\lambda^{\mathrm{g}}}{\lambda^{\max}-1}\right]^{\gamma} \quad \text{with} \quad \frac{\partial k^{\mathrm{g}}}{\partial \lambda^{\mathrm{g}}} = -\frac{\gamma}{[\lambda^{\max}-\lambda^{\mathrm{g}}]}k^{\mathrm{g}} \tag{45}$$

with parameters that have a clear micromechanical interpretation: τ denotes the adaptation speed, γ calibrates the shape of the adaptation curve, and $\lambda^{\max}$ denotes the maximum pathological cardiomyocyte stretch. The growth criterion ϕ^{g} is expressed in terms of the elastic overstretch $\lambda^{\mathrm{e}}-\lambda^{\mathrm{crit}}$,

$$\phi^{\mathrm{g}} = \lambda^{\mathrm{e}}-\lambda^{\mathrm{crit}} = \frac{\lambda}{\lambda^{\mathrm{g}}}-\lambda^{\mathrm{crit}} \quad \text{with} \quad \frac{\partial \phi^{\mathrm{g}}}{\partial \vartheta^{\mathrm{g}}} = -\frac{1}{\lambda^{\mathrm{g}2}}\lambda \tag{46}$$

such that growth is activated only if the elastic stretch $\lambda^{\mathrm{e}} = \lambda/\lambda^{\mathrm{g}}$ exceeds a critical physiological threshold value λ^{crit}. Again, we combine a classical implicit Euler backward scheme with the finite difference approximation $\dot{\lambda}^{\mathrm{g}} = [\lambda^{\mathrm{g}}-\lambda \mathrm{n}^{\mathrm{g}}]/\Delta t$, to obtain the specification of the discrete residual (15):

$$\mathrm{R} = \lambda^{\mathrm{g}}-\lambda^{\mathrm{g}}_{\mathrm{n}}-\frac{1}{\tau}\left[\frac{\lambda^{\max}-\lambda^{\mathrm{g}}}{\lambda^{\max}-1}\right]^{\gamma}\left[\frac{\lambda}{\lambda^{\mathrm{g}}}-\lambda^{\mathrm{crit}}\right]\Delta t \doteq 0. \tag{47}$$

Its linearization renders the local tangent operator (16),

$$\mathrm{K} = \frac{\partial \mathrm{R}}{\partial \lambda^{\mathrm{g}}} = 1+\left[\frac{1}{\tau}\left[\frac{\lambda^{\max}-\lambda^{\mathrm{g}}}{\lambda^{\max}-1}\right]^{\gamma}\left[\frac{\gamma}{\lambda^{\max}-\lambda^{\mathrm{g}}}\left[\frac{\lambda}{\lambda^{\mathrm{g}}}-\lambda^{\mathrm{crit}}\right]+\frac{\lambda}{\lambda^{\mathrm{g}2}}\right]\right]\Delta t \tag{48}$$

which defines the iterative update of the pathological cardiomyocyte stretch $\lambda^{\mathrm{g}} \leftarrow \lambda^{\mathrm{g}}-\mathrm{R}/\mathrm{K}$. After convergence, we can determine the growth tensor $\boldsymbol{F}^{\mathrm{g}} = \boldsymbol{I}+[\lambda^{\mathrm{g}}-1]\boldsymbol{f}_0 \otimes \boldsymbol{f}_0$ from Eq. (41), the elastic tensor $\boldsymbol{F}^{\mathrm{e}} = \boldsymbol{F}\cdot\boldsymbol{F}^{\mathrm{g}-1}$ from Eq. (1), and the elastic stress $\boldsymbol{S}^{\mathrm{e}}$ and the overall stress $\boldsymbol{S}$ from Eq. (17). Lastly, we can determine the fourth term of the consistent constitutive moduli (18) using the final equilibrium value for the pathological cardiomyocyte stretch λ^{g}:

$$\frac{\partial \vartheta^{\mathrm{g}}}{\partial \boldsymbol{C}} = \frac{\partial \vartheta^{\mathrm{g}}}{\partial \lambda}\frac{\partial \lambda}{\partial \boldsymbol{C}} = \left[\frac{k^{\mathrm{g}}}{\mathrm{K}}\Delta t\right]\left[\frac{1}{2\lambda}\boldsymbol{f}_0 \otimes \boldsymbol{f}_0\right]. \tag{49}$$

Table 2
Algorithmic treatment of strain-driven transversely isotropic growth.

given $\boldsymbol{F}$ and $\lambda^{\mathrm{g}}_{\mathrm{n}}$	
initialize $\lambda^{\mathrm{g}} \leftarrow \lambda^{\mathrm{g}}_{\mathrm{n}}$	
local Newton iteration	
check growth criterion $\phi^{\mathrm{g}} = \lambda^{\mathrm{e}} - \lambda^{\mathrm{crit}} \geq 0$?	(46)
calculate growth function $k^{\mathrm{g}} = [[\lambda^{\mathrm{max}} - \lambda^{\mathrm{g}}]/[\lambda^{\mathrm{max}} - 1]]^{\gamma}/\tau$	(45)
calculate residual $\mathsf{R} = \lambda^{\mathrm{g}} - \lambda^{\mathrm{g}}_{\mathrm{n}} - k^{\mathrm{g}}\phi^{\mathrm{g}}\Delta t$	(47)
calculate tangent $\mathsf{K} = \partial \mathsf{R}/\partial \vartheta^{\mathrm{g}}$	(48)
update growth stretch $\lambda^{\mathrm{g}} \leftarrow \lambda^{\mathrm{g}} - \mathsf{R}/\mathsf{K}$	
check convergence $\mathsf{R} \leq \mathrm{tol}$?	
calculate growth tensor $\boldsymbol{F}^{\mathrm{g}} = \boldsymbol{I} + [\lambda^{\mathrm{g}} - 1]\boldsymbol{f}_0 \otimes \boldsymbol{f}_0$	(41)
calculate elastic tensor $\boldsymbol{F}^{\mathrm{e}} = \boldsymbol{F} \cdot \boldsymbol{F}^{\mathrm{g}-1}$	(1)
calculate elastic right Cauchy Green tensor $\boldsymbol{C}^{\mathrm{e}} = \boldsymbol{F}^{\mathrm{et}} \cdot \boldsymbol{F}^{\mathrm{e}}$	(2)
calculate elastic second Piola Kirchhoff stress $\boldsymbol{S}^{\mathrm{e}} = 2\partial\psi/\partial\boldsymbol{C}^{\mathrm{e}}$	(10)
calculate second Piola Kirchhoff stress $\boldsymbol{S} = \boldsymbol{F}^{\mathrm{g}-1} \cdot \boldsymbol{S}^{\mathrm{e}} \cdot \boldsymbol{F}^{\mathrm{g}}$	(17)
calculate Lagrangian moduli L	(18) with (19), (20), (43), (49)
push forward to Kirchhoff stress $\boldsymbol{\tau} = \boldsymbol{F} \cdot \boldsymbol{S} \cdot \boldsymbol{F}^{\mathrm{t}}$	(21)
push forward to Eulerian moduli $\mathsf{e} = [\boldsymbol{F} \otimes \boldsymbol{F}] : \mathsf{L} : [\boldsymbol{F}^{\mathrm{t}} \overline{\otimes} \boldsymbol{F}^{\mathrm{t}}]$	(22)

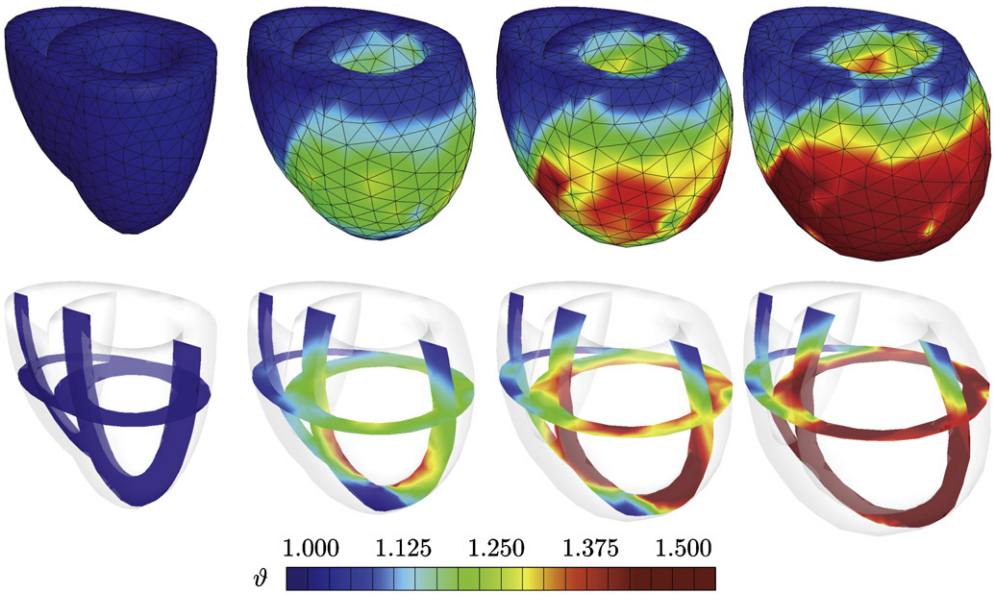

Fig. 9. Cardiac dilation, strain-driven eccentric growth, and increase in cavity size at constant wall thickness. The eccentric growth multiplier ϑ gradually increases from 1.00 to 1.50 as the individual cardiomyocytes grow eccentrically. On the macroscopic scale, cardiac dilation manifests itself in a progressive dilation of the chambers to maintain cardiac output at a physiological level while the thickness of the ventricular wall remains constant.

6.3. Algorithmic treatment of cardiac dilation

Table 2 summarizes the algorithmic treatment of strain-driven transversely isotropic growth. In contrast to stress-driven growth, the local Newton iteration is now purely kinematic. In our case, where we have introduced a single growth multiplier λ^{g}, the local Newton iteration does not even involve tensorial operations but is just scalar-valued. After the iterative computation of the growth multiplier, all other quantities can be post-processed. Recall that the overall constitutive moduli for anisotropic strain-driven growth are non-symmetric and a non-symmetric finite element solver is required to fully benefit from the quadratic convergence of the Newton Raphson scheme.

6.4. Example of cardiac dilation

The following example documents our attempts to simulate strain-driven transversely isotropic growth using our generic biventricular heart model. In addition to the specifications in Section 4, we have to specify two additional growth parameters, the physiological threshold $\lambda^{\mathrm{crit}} = 1.001$ and the maximum growth threshold $\lambda^{\mathrm{max}} = 1.50$. The simulation of cardiac dilation is illustrated in Fig. 9 in terms of the deformed configurations at end systole for four consecutive load

cycles. Characteristic for cardiac dilation, strain-driven eccentric growth manifests itself in a significant increase in cavity size at constant wall thickness. The eccentric growth multiplier λ gradually increases from its baseline value $\lambda = 1.00$ to its maximum value $\lambda^{\max} = 1.50$ as the individual cardiomyocytes grow eccentrically. On the macroscopic scale, cardiac dilation manifests itself in a progressive dilation of the chambers to maintain cardiac output at a physiological level while the thickness of the ventricular wall remains constant. In summary, the simulation illustrated in Fig. 9 is excellent qualitative agreement with the pathophysiological characteristics of cardiac dilation summarized in Section 6.1 and illustrated in Fig. 8: (i) progressive increase in cardiac diameter and mass, (ii) alteration of cardiac form from elliptical to spherical, (iii) relatively constant wall thickness, and (iv) potential development of mitral regurgitation through pronounced ventricular dilation.

7. Example cardiac wall thickening: stress-driven transversely isotropic growth

7.1. Pathophysiology of cardiac wall thickening

Cardiac wall thickening is a chronic medical condition in which the heart muscle grows transmurally in response to pressure overload while the overall size of the heart remains virtually unchanged. Downstream occlusions, e.g., caused by a calcified stenotic aortic valve, might increase the downstream resistance and induce hypertension which causes the wall to adaptively change its thickness in an attempt to maintain wall stresses at a physiological level (Opie, 2003), see Fig. 10. On the microscopic scale, increased systolic wall stresses stimulate the addition of new sacromeres in parallel to the existing sarcomere units, resulting in a relative increase in transverse cardiomyocyte diameters from 15 μm up to 40 μm (Kumar et al., 2005). On the macroscopic scale, these morphological changes result in concentric hypertrophy and the wall thickness can increase to more than 3 cm (Maron and McKenna, 2003). As such, the driving force of ventricular wall thickening is conceptually similar to wall thickening in arteries driven by hypertension (Kuhl et al., 2007). Potentially unfavorable consequences of thick ventricular walls are insufficient blood supply and impaired filling due to an increased wall stiffness. Hypertrophic obstructive wall thickening is a pathological adaptation of the heart muscle that is usually progressive and irreversible.

7.2. Governing equations of cardiac wall thickening

In our continuum growth model, we assume cardiac wall thickening to be a stress-driven, transversely isotropic, irreversible growth process. Motivated by physiological observations, we introduce a single scalar-valued growth multiplier ϑ^{g},

$$\vartheta^{\mathrm{s}} = \vartheta^{\mathrm{g}} \quad \text{and} \quad \vartheta^{\mathrm{f}} = \vartheta^{\mathrm{n}} = 1 \tag{50}$$

that reflects the parallel deposition of sarcomeres associated with transverse cardiomyocyte growth on the microscopic scale. The growth tensor can thus be expressed as a simple rank one-update of the identity tensor in the direction of the

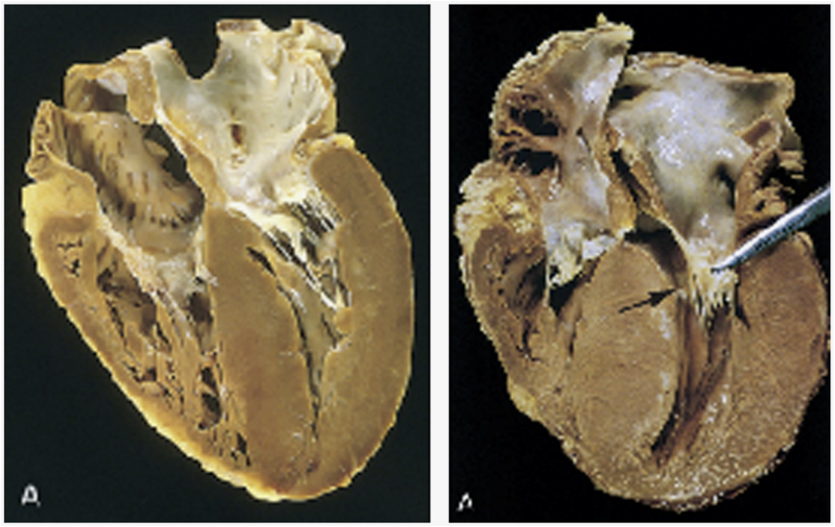

Fig. 10. Cardiac wall thickening, stress-driven concentric growth, and transmural muscle thickening at constant cardiac size, reprinted with permission from Emmanouilides et al. (1994) and Kumar et al. (2005). Left ventricular outflow obstruction has caused pressure-overload hypertrophy associated with a significant wall thickening (left). A pronounced septal hypertrophy has caused the significantly thickened septal muscle to bulge into the left ventricular outflow tract (right).

sheet vector $\boldsymbol{s}_0$:

$$\boldsymbol{F}^{\mathrm{g}} = \boldsymbol{I} + [\vartheta^{\mathrm{g}} - 1]\boldsymbol{s}_0 \otimes \boldsymbol{s}_0. \tag{51}$$

Accordingly, its inverse can be expressed explicitly using the Sherman–Morrison formula

$$\boldsymbol{F}^{\mathrm{g}-1} = \boldsymbol{I} - \frac{\vartheta^{\mathrm{g}} - 1}{\vartheta^{\mathrm{g}}}\boldsymbol{s}_0 \otimes \boldsymbol{s}_0 \tag{52}$$

and its derivative with respect to the growth multiplier ϑ^{g}, which is essentially required for the constitutive moduli in Eq. (18), is nothing but the structural tensor $\boldsymbol{s}_0 \otimes \boldsymbol{s}_0$:

$$\frac{\partial \boldsymbol{F}^{\mathrm{g}}}{\partial \vartheta^{\mathrm{g}}} = \boldsymbol{s}_0 \otimes \boldsymbol{s}_0. \tag{53}$$

Motivated by clinical observations, we introduce a stress-driven evolution equation for eccentric hypertrophic growth:

$$\dot{\vartheta}^{\mathrm{g}} = k^{\mathrm{g}}(\vartheta^{\mathrm{g}})\phi^{\mathrm{g}}(\boldsymbol{M}^{\mathrm{e}}). \tag{54}$$

To ensure that the cardiomyocytes do not thicken unboundedly, the evolution of the growth multiplier ϑ^{g} is scaled by the function k^{g}:

$$k^{\mathrm{g}} = \frac{1}{\tau}\left[\frac{\vartheta^{\max} - \vartheta^{\mathrm{g}}}{\vartheta^{\max} - 1}\right]^{\gamma} \quad \text{with} \quad \frac{\partial k^{\mathrm{g}}}{\partial \vartheta^{\mathrm{g}}} = -\frac{\gamma}{[\vartheta^{\max} - \vartheta^{\mathrm{g}}]}k^{\mathrm{g}}. \tag{55}$$

In fact the parameters of this function all have a clear physical interpretation: τ denotes the adaptation speed, γ calibrates the shape of the adaptation curve, i.e., the degree of nonlinearity of the growth process, and $\vartheta^{\max}$ denotes the area fraction of maximum parallel sarcomere deposition, e.g., $\vartheta^{\max} = \frac{8}{3}$ for a maximum cardiomyocyte width of 40 μm. Lastly, we introduce a growth criterion ϕ^{g}, similar to the athlete's heart, in a stress-driven fashion. We choose the overstress $\mathrm{tr}(\boldsymbol{M}^{\mathrm{e}}) - M^{\mathrm{e\ crit}}$, i.e., the difference of the trace of the Mandel stress of the intermediate configuration $\boldsymbol{M}^{\mathrm{e}} = \boldsymbol{C}^{\mathrm{e}} \cdot \boldsymbol{S}^{\mathrm{e}}$ and the baseline pressure level M^{crit} as the driving for growth:

$$\phi^{\mathrm{g}} = \mathrm{tr}(\boldsymbol{M}^{\mathrm{e}}) - M^{\mathrm{e\ crit}} \quad \text{with} \quad \frac{\partial \phi^{\mathrm{g}}}{\partial \vartheta^{\mathrm{g}}} = \frac{\partial \boldsymbol{C}^{\mathrm{e}}}{\partial \vartheta^{\mathrm{g}}} : \boldsymbol{S}^{\mathrm{e}} + \boldsymbol{C}^{\mathrm{e}} : \frac{\partial \boldsymbol{S}^{\mathrm{e}}}{\partial \vartheta^{\mathrm{g}}}. \tag{56}$$

However now, unlike in the isotropic growth example of the athlete's heart (29), the sensitivities

$$\frac{\partial \boldsymbol{C}^{\mathrm{e}}}{\partial \vartheta^{\mathrm{g}}} = -\boldsymbol{F}^{\mathrm{g-t}} \cdot \frac{\partial \boldsymbol{F}^{\mathrm{g\,t}}}{\partial \vartheta^{\mathrm{g}}} \cdot \boldsymbol{C}^{\mathrm{e}} - \boldsymbol{C}^{\mathrm{e}} \cdot \frac{\partial \boldsymbol{F}^{\mathrm{g}}}{\partial \vartheta^{\mathrm{g}}} \cdot \boldsymbol{F}^{\mathrm{g}-1} \quad \text{and} \quad \frac{\partial \boldsymbol{S}^{\mathrm{e}}}{\partial \vartheta^{\mathrm{g}}} = \frac{1}{2}\mathbb{L}^{\mathrm{e}} : \frac{\partial \boldsymbol{C}^{\mathrm{e}}}{\partial \vartheta^{\mathrm{g}}} \tag{57}$$

become slightly more complex, since the growth tensor $\boldsymbol{F}^{\mathrm{g}}$ is now anisotropic. Again, we apply an implicit Euler backward scheme with $\dot{\vartheta}^{\mathrm{g}} = [\vartheta^{\mathrm{g}} - \vartheta^{\mathrm{g}}_{\mathrm{n}}]/\Delta t$, to obtain the following expression for the discrete residual:

$$\mathrm{R} = \vartheta^{\mathrm{g}} - \vartheta^{\mathrm{g}}_{\mathrm{n}} - \frac{1}{\tau}\left[\frac{\vartheta^{\max} - \vartheta^{\mathrm{g}}}{\vartheta^{\max} - 1}\right]^{\gamma} [\mathrm{tr}(\boldsymbol{M}^{\mathrm{e}}) - M^{\mathrm{e\ crit}}]\Delta t \doteq 0. \tag{58}$$

The iterative update $\vartheta^{\mathrm{g}} \leftarrow \vartheta^{\mathrm{g}} - \mathrm{R}/\mathrm{K}$ of the growth multiplier can then be expressed in terms of the linearization of discrete residual (58)

$$\mathrm{K} = \frac{\mathrm{dR}}{\mathrm{d}\vartheta^{\mathrm{g}}} = 1 - \left[k^{\mathrm{g}}\frac{\partial \phi^{\mathrm{g}}}{\partial \vartheta^{\mathrm{g}}} + \phi^{\mathrm{g}}\frac{\partial k^{\mathrm{g}}}{\partial \vartheta^{\mathrm{g}}}\right]\Delta t \tag{59}$$

within a local Newton iteration, to calculate the multiplier of concentric growth ϑ^{g} for the current time step. Last, to complete the calculation of the tangent moduli (18), we determine the partial derivative of the converged growth multiplier ϑ^{g} with respect to the right Cauchy Green deformation gradient of the reference configuration $\boldsymbol{C}$,

$$\frac{\partial \vartheta^{\mathrm{g}}}{\partial \boldsymbol{C}} = \frac{\partial \vartheta^{\mathrm{g}}}{\partial \boldsymbol{C}^{\mathrm{e}}} : \frac{\partial \boldsymbol{C}^{\mathrm{e}}}{\partial \boldsymbol{C}} = \left[\frac{k^{\mathrm{g}}}{\mathrm{K}}\Delta t\right]\left[\frac{1}{2}\boldsymbol{C} : \mathrm{L}^{0} + \boldsymbol{S}\right], \tag{60}$$

where we have introduced the abbreviation

$$\mathbb{L}^{0} = [\boldsymbol{F}^{\mathrm{g}-1} \overline{\otimes} \boldsymbol{F}^{\mathrm{g}-1}] : \mathrm{L}^{\mathrm{e}} : [\boldsymbol{F}^{\mathrm{g-t}} \overline{\otimes} \boldsymbol{F}^{\mathrm{g-t}}] \tag{61}$$

for the pull back of the elastic moduli $\boldsymbol{L}^{\mathrm{e}} = 2\,\partial \boldsymbol{S}^{\mathrm{e}}/\partial \boldsymbol{C}^{\mathrm{e}}$ from the grown intermediate configuration to the undeformed reference configuration. Again, this update has structure similar to Eq. (34), but is slightly more complex due to the underlying anisotropy.

7.3. Algorithmic treatment of cardiac wall thickening

Table 3 illustrates the algorithmic treatment of stress-driven transversely isotropic growth. The algorithm is somewhat similar to the stress-driven growth algorithm for athlete's heart in Table 1, however, it is slightly more elaborate since the pull back and push forward operations are now fully tensorial. Similar to the transversely isotropic growth in cardiac

Table 3
Algorithmic treatment of stress-driven transversely isotropic growth.

given $\boldsymbol{F}$ and ϑ^{g}_{n}	
initialize $\vartheta^{g} \leftarrow \vartheta^{g}_{n}$	
local Newton iteration	
calculate growth tensor $\boldsymbol{F}^{g} = \boldsymbol{I} + [\vartheta^{g} - 1]\boldsymbol{s}_0 \otimes \boldsymbol{s}_0$	(51)
calculate elastic tensor $\boldsymbol{F}^{e} = \boldsymbol{F} \cdot \boldsymbol{F}^{g-1}$	(1)
calculate elastic right Cauchy Green tensor $\boldsymbol{C}^{e} = \boldsymbol{F}^{et} \cdot \boldsymbol{F}^{e}$	(2)
calculate second Piola Kirchhoff stress $\boldsymbol{S}^{e} = 2\partial\psi/\partial\boldsymbol{C}^{e}$	(10)
check growth criterion $\phi^{g} = \mathrm{tr}(\boldsymbol{C}^{e} \cdot \boldsymbol{S}^{e}) - M^{ecrit} \geq 0$?	(56)
calculate growth function $k^{g} = [[\vartheta^{max} - \vartheta^{g}]/[\vartheta^{max} - 1]]^{\gamma}/\tau$	(55)
calculate residual $\mathsf{R} = \vartheta^{g} - \vartheta^{g}_{n} - k^{g}\phi^{g}\Delta t$	(58)
calculate tangent $\mathsf{K} = \partial\mathsf{R}/\partial\vartheta^{g}$	(59)
update growth multiplier $\vartheta^{g} \leftarrow \vartheta^{g} - \mathsf{R}/\mathsf{K}$	
check convergence $\mathsf{R} \leq \mathrm{tol}$?	
calculate second Piola Kirchhoff stress $\boldsymbol{S} = \boldsymbol{F}^{g-1} \cdot \boldsymbol{S}^{e} \cdot \boldsymbol{F}^{g}$	(17)
calculate Lagrangian moduli L	(18) with (19), (20), (53), (60)
push forward to Kirchhoff stress $\boldsymbol{\tau} = \boldsymbol{F} \cdot \boldsymbol{S} \cdot \boldsymbol{F}^{t}$	(21)
push forward to Eulerian moduli $\mathbf{e} = [\boldsymbol{F}\overline{\otimes}\boldsymbol{F}] : \mathsf{L} : [\boldsymbol{F}^{t}\overline{\otimes}\boldsymbol{F}^{t}]$	(22)

dilation, our constitutive moduli now become non-symmetric such that a non-symmetric finite element solver is required to ensure quadratic convergence and maximize computational efficiently.

7.4. Example of cardiac wall thickening

Our last example illustrates the performance of the growth algorithm in the context of stress-driven transversely isotropic growth using our generic biventricular heart model. Again, the geometry, boundary conditions, and loading are adopted from Section 4. The two additional growth parameters are the physiological threshold $M^{e\ crit} = 0.012$ MPa and the maximum growth threshold $\vartheta^{max} = 3.00$. Fig. 11 documents the resulting deformed configurations at end systole for four consecutive load cycles. Cardiac wall thickening is characterized through stress-driven concentric growth, and transmural muscle thickening at constant cardiac size. The concentric growth multiplier ϑ gradually increases from $\vartheta = 1.00$ to $\vartheta^{max} = 3.00$ as the individual cardiomyocytes grow concentrically. On the macroscopic scale, wall thickening manifests itself in a progressive transmural muscle growth to withstand higher blood pressure levels while the overall size of the heart remains constant. Accordingly, there are two mechanisms that can potentially slow down the accumulation of further growth, one is rather algorithmic and associated with the growth multiplier having reached its prescribed value of ϑ^{max}, the other one is rather physiological and associated with the reduction of the wall stresses $\mathrm{tr}(\boldsymbol{C}^{e} \cdot \boldsymbol{S}^{e})$ below the critical threshold $M^{e\ crit} = 0.012$ MPa. The heterogeneous stress profile triggers a heterogeneous progression of growth: since the septal wall receives structural support through the pressure in the right ventricle, wall thickening is slightly more pronounced at the free wall where the wall stresses are higher. In summary, the simulation illustrated in Fig. 11 is excellent qualitative agreement with the pathophysiological characteristics of cardiac wall thickening discussed in Section 7.1 and illustrated in Fig. 10: (i) progressive wall thickening, (ii) relatively constant heart size, and (iii) potential occlusion of the outflow tract through pronounced septal growth.

8. Discussion

Adopting the concept of an incompatible configuration to characterize volumetric growth of biological tissue is a commonly accepted approach in the biomechanics community. Within the last decade, a tremendous amount of research has been devoted to better understand the kinematics of growth, to reformulate the underlying balance equations, and to introduce appropriate constitutive equations for growing tissue (Ambrosi et al., under review). Yet, two fundamental problems remain unanswered: the kinematic definition of the growth tensor and the identification of the mechanical driving forces for growth. In this manuscript, we have presented an attempt to closely tie both quantities to the microstructural architecture of the underlying tissue. We have illustrated this concept for one particular type of tissue, the myocardial muscle. After establishing the continuous and discrete equations for finite growth, we have specified different growth tensors and driving forces for three distinct pathophysiological cases: athlete's heart, cardiac dilation, and cardiac wall thickening. For each case, we have introduced the appropriate growth tensor, either isotropic or anisotropic, and the mechanical driving force, either stress or strain. We have shown how the underlying equations can be embedded within the concept of internal variables, and have solved the evolution equations of growth using a local Newton Raphson iteration. Simulations related to all three cases have been in excellent qualitative agreement with the corresponding pathophysiological observations, and have been able to capture characteristic effects such as volume overload induced dilation, pressure overload induced wall thickening, and combinations thereof.

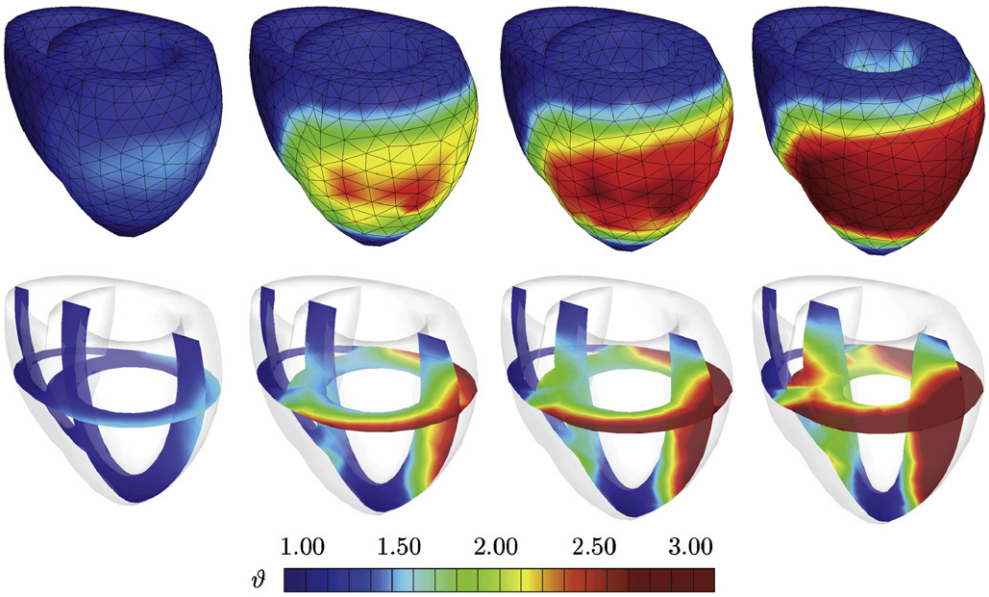

Fig. 11. Cardiac wall thickening, stress-driven concentric growth, and transmural muscle thickening at constant cardiac size. The concentric growth multiplier ϑ gradually increases from 1.00 to 3.00 as the individual cardiomyocytes grow concentrically. On the macroscopic scale, cardiac wall thickening manifests itself in a progressive transmural muscle growth to withstand higher blood pressure levels while the overall size of the heart remains constant. Since the septal wall receives structural support through the pressure in the right ventricle, wall thickening is slightly more pronounced at the free wall where the wall stresses are higher.

Despite the tremendous potential of the proposed approach, we would like to point out several limitations related to the transformative nature towards a reliable, predictive, clinically applicable model. First, in our models system, growth is attributed exclusively to kinematic changes of one particular cell type. This approach seems reasonable for the heart, since its volume is made up almost exclusively of cardiomyocytes which are unable to divide and can only grow in size. The heart therefore represents an extremely unique and elegant model system to study volumetric growth. Second, to focus on the impact of growth, we have used a relatively simple and easily reproducible finite element prototype model with several conceptual limitations: (i) The baseline elasticity has been assumed to be isotropic of Neo-Hookean type. However, the incorporation of a more physiological anisotropic baseline elasticity is straightforward and part of our current research efforts (Göktepe et al., 2010b). (ii) The choice of boundary conditions might have a significant impact on the growth profile. For the lack of better knowledge, we have fixed the entire basal plane, and thereby prevented the annulus from dilating. In a more realistic model, more physiological boundary conditions should be incorporated to allow us to predict the impact of cardiac dilation on functional mitral regurgitation (Göktepe et al., 2010c). (iii) For the sake of simplicity, we have only modeled the passive effects of ventricular filling. In order to clearly distinguish between systolic and diastolic heart diseases, it is important to incorporate the effects of active cardiomyocyte contraction (Göktepe and Kuhl, 2010). This will also allow us to more precisely distinguish between the effects of pressure and volume overload. (iv) The present study has been based on a generic biventricular geometry in which the fiber orientation can be specified parametrically. Replacing this geometry by more realistic patient specific geometries in itself is relatively straightforward (Kotikanyadanam et al., 2010). A current challenge, however, is the incorporation of realistic fiber geometries, acquired, for example, with the help of diffusion tensor MRI. (v) This manuscript is mainly a proof of concept and we have not yet addressed the issue of calibrating the time parameters of the model. We envision first utilizing chronic animal models to characterize the evolution of growth over time and then compare the findings with long term studies of cardiac growth in humans (Cheng et al., 2006).

In summary, in this manuscript, we have established a novel generic approach towards finite growth in which growth is directly related to the underlying cellular microstructure. When calibrated appropriately, this approach will allow us to better understand the microscopic and macroscopic mechanisms of chronic cardiac disease related to the maladaptation of the heart muscle. Current therapies for cardiac repair seek to structurally support the failing heart through passive support devises. Stem cell therapies have demonstrated the potential to not only provide passive support, but to also restore active mechanical function. A computational model based on the proposed framework for finite growth could help to systematically improve passive support devices or optimize injection sites for stem cell delivery. Overall, the continuum modeling and computational simulation of growing biological tissue represents an exciting and challenging field through which classical mechanics could have a tremendous impact on shaping quantitative, predictive research in life sciences and medicine.

Acknowledgements

This material is based on work supported by the National Science Foundation CAREER award CMMI-0952021 "The Virtual Heart—Exploring the structure-function relationship in electroactive cardiac tissue", by the Hellman Faculty Scholars grant "A predictive multiscale simulation tool for heart failure", by the Stanford Bio-X grant "An integrated approach to cardiac repair: Predictive computational models, engineered biomaterials, and stem cells", and by the National Science Foundation ERFI program through Grant EFRI-CBE-0735551 "Engineering of cardiovascular cellular interfaces and tissue constructs".

References

Alastrue, V., Martinez, M.A., Doblare, M., 2009. Modelling adaptative volumetric finite growth in patient-specific residually stressed arteries. J. Biomech. 41, 1773–1781.
Alford, P.W., Taber, L.A., 2008. Computational study of growth and remodelling in the aortic arch. Comput. Meth. Biomech. Biomed. Eng. 11, 525–538.
Ambrosi, D., Mollica, F., 2002. On the mechanics of a growing tumor. Int. J. Eng. Sci. 40, 1297–1316.
Ambrosi, D., Guillou, A., Di Martino, E.S., 2008. Stress-modulated remodeling of a non-homogeneous body. Biomech. Model. Mechanobiol. 7, 63–76.
Ambrosi, D., Ateshian, G.A., Arruda, E.M., Ben Amar, M., Cowin, S.C., Dumais, J., Goriely, A., Holzapfel, G.A., Humphrey, J.D., Kemkemer, R., Kuhl, E., Ma, J., Olberding, J.E., Taber, L.A., Vandiver, R., Garikipati, K., under review. Perspectives on biological growth and remodeling.
Ben Amar, M., Goriely, A., 2005. Growth and instability in elastic tissues. J. Mech. Phys. Solids 53, 2284–2319.
Berne, R.M., Levy, M.N., 2001. Cardiovascular Physiology. The Mosby Monograph Series.
Boyce, M.C., Weber, G.G., Parks, D.M., 1989. On the kinematics of finite strain plasticity. J. Mech. Phys. Solids 37, 647–665.
Carter, D.R., Hayes, W.C., 1977. The behavior of bone as a twophase porous structure. J. Bone Jt. Surg. 59, 785–794.
Chen, Y.C., Hoger, A., 2000. Constitutive functions of elastic materials in finite growth and deformation. J. Elast. 59, 175–193.
Cheng, A., Nguyen, T.C., Malinowski, M., Ennis, D.B., Daughters, G.T., Miller, D.C., Ingels, N.B., 2006. Transmural left ventricular shear strain alterations adjacent to and remote from infarcted myocardium. J. Heart Valve Dis. 15, 209–218.
Ciarletta, P., Ben Amar, M., 2009. A finite dissipative theory of temporary interfibrillar bridges in the extracellular matrix of ligaments and tendons. J. R. Soc. Interface 6, 909–924.
Cowin, S.C., Hegedus, D.H., 1976. Bone remodeling. 1. Theory of adaptive elasticity. J. Elast. 6, 313–326.
Cowin, S.C., 2004. Tissue growth and remodeling. Ann. Rev. Biomed. Eng. 6, 77–107.
Dumais, J., Shaw, S.L., Steele, C.R., Long, S.R., Ray, P.M., 2006. An anisotropic–viscoplastic model of plant cell morphogenesis by tip growth. Int. J. Dev. Biol. 50, 209–222.
Emmanouilides, G.C., Riemenschneider, R.A., Allen, H.D., Gutgesell, H.P., 1994. Moss and Adams' Heart Disease in Infants, Children, and Adolescents, fifth ed. Lippincott Williams & Wilkins.
Epstein, M., Maugin, G.A., 2000. Thermomechanics of volumetric growth in uniform bodies. Int. J. Plast. 16, 951–978.
Ekblom, B., Hermansen, L., 1968. Cardiac output in athletes. J. Appl. Physiol. 25, 619–625.
Figueroa, C.A., Baek, S., Taylor, C.A., Humphrey, J.D., 2009. A computational framework for fluid–solid-growth modeling in cardiovascular simulations. Comput. Meth. Appl. Mech. Eng. 198, 3583–3602.
Garciarena, C.D., Pinilla, O.A., Nolly, M.B., Laguens, R.P., Escudero, E.M., Cingolani, H.E., Ennis, I.L., 2009. Endurance training in the spontaneously hypertensive rat: conversion of pathological into physiological cardiac hypertrophy. Hypertension 53, 708–714.
Garikipati, K., Arruda, E.M., Grosh, K., Narayanan, H., Calve, S., 2004. A continuum treatment of growth in biological tissue: the coupling of mass transport and mechanics. J. Mech. Phys. Solids 52, 1595–1625.
Garikipati, K., 2009. The kinematics of biological growth. Appl. Mech. Rev. 62, 030801-1–030801-7.
Göktepe, S., Kuhl, E., 2009. Computational modeling of cardiac electrophysiology: a novel finite element approach. Int. J. Numer. Meth. Eng. 79, 156–178.
Göktepe, S., Kuhl, E., 2010. Electromechanics of cardiac tissue: a unified approach to the fully coupled excitation–contraction problem. Comput. Mech. 45, 227–243.
Göktepe, S., Abilez, O.J., Parker, K.K., Kuhl, E., 2010a. A multiscale model for eccentric and concentric cardiac growth through sarcomerogenesis. J. Theor. Biol. 265, 433–442.
Göktepe, S., Acharya, S.N.S., Wong, J., Kuhl, E., 2010b. Computational modeling of passive myocardium. Int. J. Numer. Meth. Biomed. Eng., doi:10.1002/cnm.1402.
Göktepe, S., Bothe, W., Kvitting, J.P., Swanson, J.C., Ingels, N.B., Miller, D.C., Kuhl, E., 2010c. Anterior mitral leaflet curvature in the beating ovine heart: a case study using video fluoroscopic markers and subdivision surfaces. Biomech. Model. Mechanobiol. 9, 281–293.
Goriely, A., Ben Amar, M., 2007. On the definition and modeling of incremental, cumulative, and continuous growth laws in morphoelasticity. Biomech. Model. Mechanobiol. 6, 289–296.
Himpel, G., Kuhl, E., Menzel, A., Steinmann, P., 2005. Computational modeling of isotropic multiplicative growth. Comput. Mod. Eng. Sci. 8, 119–134.
Himpel, G., Menzel, A., Kuhl, E., Steinmann, P., 2008. Time-dependent fibre reorientation of transversely isotropic continua—finite element formulation and consistent linearization. Int. J. Numer. Meth. Eng. 73, 1413–1433.
Holzapfel, G.A., Ogden, R.W., 2009. Constitutive modelling of passive myocardium. A structurally-based framework for material characterization. Philos. Trans. R. Soc. London A 367, 3445–3475.
Hsu, H.F., 1968. The influence of mechanical loads on the form of a growing elastic body. J. Biomech. 1, 303–311.
Humphrey, J.D., 2002. Cardiovascular Solid Mechanics. Springer Verlag, Berlin, Heidelberg, New York.
Humphrey, J.D., Rajagopal, K.R., 2002. A constrained mixture model for growth and remodeling of soft tissues. Math. Mod. Meth. Appl. Sci. 12, 407–430.
Humphrey, J.D., 2008. Vascular adaptation and mechanical homeostasis at tissue, cellular, and sub-cellular levels. Cell. Biochem. Biophys. 50, 53–78.
Hunter, J.J., Chien, K.R., 1999. Signaling pathways for cardiac hypertrophy and failure. New England J. Med. 341, 1276–1283.
Imatani, S., Maugin, G.A., 2002. A constitutive model for material growth and its application to three-dimensional analysis. Mech. Res. Commun. 29, 477–483.
Klisch, S.M., Chen, S.S., Hoger, A., 2003. A growth mixture theory for cartilage with application to growth-related experiments on cartilage explants. J. Biomech. Eng. 125, 169–179.
Kotikanyadanam, M., Göktepe, S., Kuhl, E., 2010. Computational modeling of electrocardiograms—a finite element approach towards cardiac excitation. Commun. Numer. Meth. Eng. 26, 524–533.
Kroon, W., Delhaas, T., Arts, T., Bovendeerd, P., 2009. Computational modeling of volumetric soft tissue growth: application to the cardiac left ventricle. Biomech. Model. Mechanobiol. 8, 309–310.
Kuhl, E., Steinmann, P., 2003a. Mass- and volume specific views on thermodynamics for open systems. Proc. Royal Soc. 459, 2547–2568.
Kuhl, E., Steinmann, P., 2003b. On spatial and material settings of thermohyperelastodynamics for open systems. Acta Mech. 160, 179–217.
Kuhl, E., Menzel, A., Steinmann, P., 2003. Computational modeling of growth—a critical review, a classification of concepts and two new consistent approaches. Comp. Mech. 32, 71–88.
Kuhl, E., Steinmann, P., 2003c. Theory and numerics of geometrically non-linear open system mechanics. Int. J. Numer. Meth. Eng. 58, 1593–1615.

Kuhl, E., Garikipati, K., Arruda, E.M., Grosh, K., 2005. Remodeling of biological tissue: mechanically induced reorientation of a transversely isotropic chain network. J. Mech. Phys. Solids 53, 1552–1573.
Kuhl, E., Maas, R., Himpel, G., Menzel, A., 2007. Computational modeling of arterial wall growth: attempts towards patient-specific simulations based on computer tomography. Biomech. Mod. Mechanobiol. 6, 321–331.
Kuhl, E., Holzapfel, G.A., 2007. A continuum model for remodeling in living structures. J. Mat. Sci. 2, 8811–8823.
Kumar, V., Abbas, A.K., Fausto, N., 2005. Robbins and Cotran Pathologic Basis of Disease. Elsevier Saunders.
Lee, E.H., 1969. Elastic-plastic deformation at finite strains. J. Appl. Mech. 36, 1–6.
Libby, P., Bonow, R.O., Mann, D.L., Zipes, D.P., 2007. Braunwald's Heart Disease, Saunders.
Lubarda, A., Hoger, A., 2002. On the mechanics of solids with a growing mass. Int. J. Solids Structures 39, 4627–4664.
Maron, B.J., McKenna, W.J., 2003. American College of Cardiology/European Society of Cardiology: clinical expert consensus document on hypertrophy cardiomyopathy. J. Am. College Cardiology 42, 1687–1713.
Maron, B.J., Pelliccia, A., 2006. The heart of trained athletes: cardiac remodeling and the risks of sports, including sudden death. Circ. 114, 1633–1644.
Menzel, A., 2005. Modelling of anisotropic growth in biological tissues—a new approach and computational aspects. Biomech. Model. Mechanobiol. 3, 147–171.
Mihl, C., Dassen, W.R.M., Kuipers, H., 2008. Cardiac remodelling: concentric versus eccentric hypertrophy in strength and endurance athletes. Nederlands Heart J. 16, 129–133.
Naghdi, P., 1990. A critical review of the state of finite plasticity. J. Appl. Math. Phys. 41, 315–394.
Opie, L.H., 2003. Heart Physiology: From Cell to Circulation. Lippincott Williams & Wilkins.
Pluim, B.M., Zwinderman, A.H., van der Laarse, A., van der Wall, E.E., 2000. The athlete's heart: a meta-analysis of cardiac structure and function. Circulation 101, 336–344.
Rodriguez, E.K., Hoger, A., McCulloch, A.D., 1994. Stress-dependent finite growth in soft elastic tissues. J. Biomech. 27, 455–467.
Sedehi, D., Ashley, E.A., 2010. Defining the limits of athlete's heart: implications for screening in diverse populations. Circulation 121, 1066–1068.
Skalak, R., 1981. Growth as a finite displacement field. In: Carlson, D.E., Shield, R.T., (Eds.), IUTAM Symposium on Finite Elasticity. Martinus Nijhoff, pp. 347–355.
Skalak, R., Farrow, D.A., Hoger, A., 1997. Kinematics of surface growth. J. Math. Biol. 35, 869–907.
Taber, L.A., 1995. Biomechanics of growth, remodeling and morphogenesis. Appl. Mech. Rev. 48, 487–545.
Taber, L.A., Humphrey, J.D., 2001. Stress-modulated growth, residual stress, and vascular heterogeneity. J. Biomech. Eng. 123, 528–535.
Thompson, A.W., 1917. On Growth and Form. Cambridge University Press.
Xiao, H., Bruhns, O.T., Meyers, A., 2006. Elastoplasticity beyond small deformations. Acta. Mech. 182, 31–111.